

# How supernova explosions power galactic winds

Peter Creasey,<sup>1</sup>★ Tom Theuns<sup>1,2</sup> and Richard G. Bower<sup>1</sup>

<sup>1</sup>*Institute for Computational Cosmology, Department of Physics, University of Durham, South Road, Durham DH1 3LE*

<sup>2</sup>*Department of Physics, University of Antwerp, Campus Groenenborger, Groenenborgerlaan 171, B-2020 Antwerp, Belgium*

Accepted 2012 November 19. Received 2012 November 6; in original form 2012 April 27

## ABSTRACT

Feedback from supernovae is an essential aspect of galaxy formation. In order to improve subgrid models of feedback, we perform a series of numerical experiments to investigate how supernova explosions shape the interstellar medium (ISM) in a disc galaxy and power a galactic wind. We use the `FLASH` hydrodynamic code to model a simplified ISM, including gravity, hydrodynamics, radiative cooling above  $10^4$  K and star formation that reproduces the Kennicutt–Schmidt relation. By simulating a small patch of the ISM in a tall box perpendicular to the disc, we obtain subparsec resolution allowing us to resolve individual supernova events. The hot interiors of supernova explosions combine into larger bubbles that sweep-up the initially hydrostatic ISM into a dense, warm cloudy medium, enveloped by a much hotter and tenuous medium, all phases in near pressure equilibrium. The unbound hot phase develops into an outflow with wind speed increasing with distance as it accelerates from the disc. We follow the launch region of the galactic wind, where hot gas entrains and ablates warm ISM clouds leading to significantly increased mass loading of the flow, although we do not follow this material as it interacts with the galactic halo.

We run a large grid of simulations in which we vary gas surface density, gas fraction and star formation rate in order to investigate the dependencies of the mass loading,  $\beta \equiv \dot{M}_{\text{wind}}/\dot{M}_*$ . In the cases with the most effective outflows, we observe  $\beta = 4$ ; however, in other cases we find  $\beta \ll 1$ . We find that outflows are more efficient in discs with lower surface densities or gas fractions. A simple model in which the warm cloudy medium is the barrier that limits the expansion of the blast wave reproduces the scaling of outflow properties with disc parameters at high star formation rates. We extend the scaling relations derived from an ISM patch to infer an effective mass loading for a galaxy with an exponential disc, finding that the mass loading depends on circular velocity as  $\beta \propto V_d^{-\alpha}$  with  $\alpha \approx 2.5$  for a model which fits the Tully–Fisher relation. Such a scaling is often assumed in phenomenological models of galactic winds in order to reproduce the flat faint end slope of the mass function. Our normalization is in approximate agreement with observed estimates of the mass loading for the Milky Way. The scaling we find sets the investigation of galaxy winds on a new footing, providing a physically motivated subgrid description of winds that can be implemented in cosmological hydrodynamic simulations and phenomenological models.

**Key words:** hydrodynamics – methods: numerical – galaxies: formation – galaxies: ISM.

## 1 INTRODUCTION

Feedback is an essential aspect of galaxy formation models. It is invoked to suppress the formation of large numbers of small galaxies (Rees & Ostriker 1977; White & Rees 1978; White & Frenk 1991). While photoheating can suppress star formation in the smallest haloes, it cannot explain the low efficiency of star formation in

haloes more massive than  $10^9 M_\odot$  (Efstathiou 1992; Okamoto, Gao & Theuns 2008). Feedback is also invoked to explain why such a small fraction of the baryons are in stars today (Fukugita, Hogan & Peebles 1998; Balogh et al. 2001). An efficient feedback implementation also appears essential for simulations to produce realistic looking disc galaxies (Scannapieco et al. 2011; McCarthy et al. 2012). Observations of galactic winds at low (Heckman, Armus & Miley 1990; Heckman et al. 2000) and high  $z \sim 3$  redshift (Pettini et al. 2001) do show gas with a range of temperature and densities moving with large velocities of hundreds of  $\text{km s}^{-1}$  with

★ E-mail: p.e.creasey.00@gmail.com

respect to the galaxy's stars, although the interpretation in terms of mass loss is complicated by the multi-phase nature of the wind (see e.g. Veilleux, Cecil & Bland-Hawthorn 2005 for a recent review). Complimentary evidence for outflows comes from the high metal abundance detected in the intergalactic medium (IGM; Cowie et al. 1995), even at low densities (Schaye et al. 2003; Aguirre et al. 2004). Numerical simulations make it plausible that galactic winds are responsible for this metal enrichment (Cen & Ostriker 1999; Aguirre et al. 2001, 2005; Theuns et al. 2002; Oppenheimer & Davé 2006; Tescari et al. 2011), with low-mass galaxies dominating the enrichment of the bulk of the IGM (Booth et al. 2012).

The sheer amount of energy released by supernovae (SNe) makes the injection of energy into the interstellar medium (ISM) by SN explosions a prime candidate for driving galactic winds (Dekel & Silk 1986). However, it is challenging to understand in detail how SNe regulate the transfer of mass and energy between the different phases of the ISM, as envisaged in the model of McKee & Ostriker (1977), and how and when this leads to the emergence of a galactic wind. Efstathiou (2000) and Silk (2001) extend the McKee & Ostriker (1977) model to examine how such interactions lead to self-regulation of star formation. They show that the properties of the galactic wind can be broadly understood once a temperature and a density for the hot phase are found. This requires a model of evaporation of cold and warm clouds, yet without a more detailed understanding of the geometry and turbulence, we can go little further than steady spherically symmetric conduction models, which go back to Cowie & McKee (1977). Even if feedback is indeed due to SNe, it is not yet clear whether this is a consequence of their injection of hot gas, of turbulence (Mac Low & Klessen 2004; Scannapieco & Brüggén 2010), of cosmic rays (Jubelgas et al. 2008), of the combined effects of magnetic fields, cosmic rays and the galaxy's differential rotation (Kulpa-Dybeł et al. 2011) or all of the above.

Full hydrodynamic modelling of the interplay between the various components of the ISM in a Milky Way (MW) like galaxy in a proper cosmological context is not yet currently possible due to the large range of scales involved, with density ranging from  $4 \times 10^{-31} \text{ g cm}^{-3}$  outside of haloes to  $\sim 10^{-20} \text{ g cm}^{-3}$  in cold clouds, temperatures from a few Kelvin inside star-forming regions to  $\sim 10^8 \text{ K}$  inside SN remnants, and time-scales from a few thousand years for the propagation of an SN blast wave inside the ISM to  $\sim 10^{10}$  years for the age of the Galaxy. Excitingly, such full hydrodynamical modelling begins to be possible for higher redshift dwarfs (e.g. Wise & Abel 2008), but for the moment models of larger galaxies at  $z \sim 0$  are limited to simulating a patch of galactic disc. In addition, we would also like to identify and understand the physics that is important in driving material from the galactic disc, and so it is desirable to have a series of numerical experiments. This is the approach we will follow in this paper.

We begin by discussing constraints on galactic winds derived from current theoretical models of galaxy formation, and place our work in the context of comparable approaches. In Section 3, we introduce the set-up of our own simulations. Briefly, we use a very simple model of the ISM which neglects the cold phase, and which is stirred by hot gas injected by SN explosions. Next we demonstrate that our subpc simulations have sufficient resolution to resolve individual explosions, and illustrate the behaviour of both the ISM and the wind for a reference model with properties chosen to be similar to that of the solar neighbourhood. In Section 5, we vary the properties of the simulated ISM (total and gas surface densities, star formation rate, cooling rate), and investigate if and when a wind is launched, and how its properties depend on that of

the ISM. We obtain scaling relations of the wind to the ISM and apply them in Section 6 to predict wind properties for a full galactic disc, and investigate how the wind properties depend on the galaxy properties. We summarize in Section 7.

## 2 CONSTRAINTS ON GALACTIC WINDS

### 2.1 Model requirements and observations

We will assume that the baryon fraction in MW-sized haloes, and haloes of lower mass, falls significantly below the cosmological value,  $f_b = \Omega_b / \Omega_M$ , due to the action of a galactic wind. Let the gaseous mass outflow rate from this wind be  $\dot{M}_{\text{wind}}$  and the star formation rate be  $\dot{M}_*$ . A simple way to parametrize the efficiency of the SN-driven wind in removing baryons from the halo is its *mass loading*, i.e. the ratio

$$\hat{\beta} \equiv \frac{\dot{M}_{\text{wind}}}{\dot{M}_*}, \quad (1)$$

where our  $\hat{\beta}$  is equivalent to the  $\beta$  of Stringer et al. (2011). We introduce the hat in order to distinguish the average mass loading for a galaxy,  $\hat{\beta}$ , from a local mass loading  $\beta$  at some point on the disc. If a galaxy exhausts its gas supply in star formation (and does not recycle wind material) then we will be left with a gas-poor galaxy with baryon fraction reduced by a factor of  $1/(1 + \hat{\beta})$ .

In order to infer the fraction of baryons ejected from galaxies, we can use the statistics of galaxies and dark matter haloes. The number density of haloes as a function of their mass can be approximated for masses below the exponential cut-off scale as a power law (Press & Schechter 1974; Reed et al. 2007):

$$\frac{dn}{d \log M} \propto M^{-0.9}. \quad (2)$$

Contrast this with the slope of the galaxy stellar mass function at low masses,

$$\frac{dn}{d \log M_*} \propto M_*^{1+\alpha}, \quad (3)$$

where observationally  $\alpha$  is found to be in the range  $[-1.5, -1]$  (see e.g. Blanton et al. 2003, 2005; Baldry et al. 2005, 2012; Li & White 2009). Naively identifying each dark matter halo with a galaxy of a given stellar mass (e.g. Guo et al. 2010) yields a galaxy-mass to halo-mass relation of  $M_* \propto M^{-0.9/(\alpha+1)}$ . Identifying the stars as the main baryonic component implies a mass loading that scales with halo mass relatively steeply as (see also Stringer et al. 2011)

$$1 + \hat{\beta} = f_b \frac{M}{M_*} \propto M^{(1.9+\alpha)/(1+\alpha)} \propto M^{-0.8}, \quad (4)$$

where we substituted a faint end slope of  $\alpha = -1.5$  to derive the last exponent. Notably, this exponent  $\rightarrow \infty$  as  $\alpha \rightarrow -1$  and falls to zero as  $\alpha \rightarrow -1.9$ , as such it is rather poorly constrained even by a well-measured slope of the galaxy stellar mass function at low masses. One can infer not only that at low masses the mass loading  $\hat{\beta} \gg 1$ , but also that it is strongly increasing towards lower mass galaxies.

Assume star formation results in the explosion of  $\varepsilon_{100}$  SNe per  $100 M_\odot$  of stars formed, each with energy  $E_{\text{SN}}$ , and that a fraction  $\eta_T$  gets converted into kinetic energy of an outflow. Neglecting other sources of energy then implies that

$$\hat{\beta} v_{\text{wind}}^2 = 2(710 \text{ km s}^{-1})^2 \eta_T \varepsilon_{100} \frac{E_{\text{SN}}}{10^{51} \text{ erg}}, \quad (5)$$

where  $v_{\text{wind}}$  is the wind speed. If  $\varepsilon_{100}$ , the thermalization factor,  $\eta_T$  and  $\varepsilon_{\text{SN}}$  are all constants, then the product  $\beta v_{\text{wind}}^2$  is also a constant. In this case, large values of  $\beta$  imply lower wind speeds, and vice versa. If the mass loading  $\beta$  indeed increases with decreasing halo mass, then of course eventually  $\beta$  may become so large that the wind can no longer escape from the galaxy's potential well. Such small haloes may be subject to other destructive mechanisms, such as evaporation by re-ionization or obliteration by the explosions of the first stars. For massive haloes, in order for the wind to escape it requires high wind speeds, implying low mass loading. The semi-analytical model of galaxy formation presented recently by Bower, Benson & Crain (2012) imposes similar constraints on galactic winds to obtain fits to the faint end of the galaxy mass function as inferred from our naive expectations; galactic winds need to have values of the mass loading  $\beta \sim 1$  for MW-like galaxies, with an indication that  $\beta$  increases even further towards lower masses. The best-fitting models have  $\beta \sim 10$  giving  $v_{\text{wind}} \sim 300 \text{ km s}^{-1}$ .

Numerical simulations of galaxy formation also try to implement galactic winds with similar properties. Cosmological simulations such as Oppenheimer & Davé (2008) essentially implement the mass loading by hand by decoupling the winds from the surrounding gas. More advanced techniques impose some constraints during the early stages of a burst of star formation when it is beneath the simulation resolution, but later allow the gas distribution to evolve normally and the mass loading to emerge. Progress in this area has been made by simulations such as Dubois & Teyssier (2008) and Shen, Wadsley & Stinson (2010). Generally these include efficient feedback in an effort to produce a reasonable galaxy population, although they struggle to produce significant winds to remove enough baryons from MW-sized galaxies.

The OWLS simulations (Schaye et al. 2010) examined a variety of feedback prescriptions and models with efficient feedback in terms of a strong galactic winds fit a variety of properties of the galaxy population, including the Tully–Fisher relation (McCarthy et al. 2012). However, in such models the properties of the winds are still part of the subgrid modelling, i.e. the wind's properties are not computed but rather are simply imposed. This is required since the mass of gas entrained by a single SN is a tiny fraction of the mass resolution element of the simulation (Creasey et al. 2011).

In order to directly simulate the *generation* of galactic winds requires a much higher resolution than can be reached in current cosmological simulations, as the sites of energy injection must be resolved (discussed further in Section 3). In order to relax these constraints, many simulators have either moved to high redshift (where the volumes are smaller) or modified the SNe in some way (such as aggregation of the energy injection). Examples of the former include Mac Low & Ferrara (1999), Fujita et al. (2004), Wise & Abel (2008) and Powell, Slyz & Devriendt (2011), all of which struggle to produce mass loadings above unity except Wise & Abel (2008), who had massive Population III progenitors for their SNe. Examples of the latter include Dubois & Teyssier (2008) and Hopkins, Quataert & Murray (2011) with similar results, although Hopkins et al. (2011) saw significant improvement by including the winds from massive stars.

Despite having a different focus, there are also a number of studies of a high-resolution SN-driven ISM which have similar set-up to the current work, although they do not investigate the properties of their winds. Joung & Mac Low (2006), Joung, Mac Low & Bryan (2009), Hill et al. (2012) and whilst this paper was being prepared Gent et al. (2012) have all modelled an SN-driven ISM in a column through a galactic disc, driving a vertical wind. These studies investigate the structure of the ISM; however, their wind

properties appear qualitatively similar to ours. On larger scales, Strickland & Stevens (2000) and Cooper et al. (2008) have extended these to an approximation of the galaxy M82, although again the resolution restrictions severely limit the simulation time and SN energy injection prescription.

There are compelling theoretical reasons to expect a high mass loading in galaxy winds, but are such winds seen in practise? The observational evidence for galactic outflows, at least in *starburst galaxies*, is extremely strong (Heckman et al. 1990, 2000; Pettini et al. 2001; Martin, Kobulnicky & Heckman 2002; Martin 2005; Strickland & Heckman 2009). Unfortunately, it is notoriously difficult to constrain the wind properties from the data directly, partly because of uncertain metallicity and ionization corrections needed to translate between the observed ion outflow and inferred total wind values, and partly because observing the wind in the spectrum of its galaxy does not provide spatial information of where the absorbing gas is located (Bouche et al. 2011, but see Wilman et al. 2005; Swinbank et al. 2009 for a few cases of resolved studies of winds). The outflowing gas is likely multi-phase in nature, complicating further the interpretation of the data. The picture for non-starburst galaxies is even more complex, with Strickland & Heckman (2009) noting the lack of evidence for superwinds in such galaxies. As Chen et al. (2010) point out, however, evidence for the high-velocity outflows come from blueshifted absorbers such as Na D that are tracing cooler material which is a fraction of the wind (or Mg II, e.g. Weiner et al. 2009 in the Deep2 galaxies). As far as it can be measured, the velocity of the outflow seems to be only weakly dependent on the star formation rate (Rupke, Veilleux & Sanders 2005). Probing the circumgalactic medium around galaxies with a sightline to a background quasar allowed Bouche et al. (2011) to infer values of  $\beta = 2\text{--}3$  and wind speeds  $v_{\text{wind}} = 150\text{--}300 \text{ km s}^{-1}$  for a set of  $L_*$  galaxies at redshift  $z \sim 0.1$ . They claim that these wind speeds are in fact below the escape speed, and hence we may be observing a galactic fountain rather than a proper outflow.

The picture of SNe as the driver of galactic winds also has consequences in terms of the metallicity of the galaxy. As SNe inject both metals and energy we expect and find a corresponding metallicity deficit for low-mass galaxies (Tremonti et al. 2004), interest in which goes back to Larson (1974). Both simple models (Peebles & Shankar 2011; Dayal, Ferrara & Dunlop 2012) and simulations (Finlator & Davé 2008) show that galactic winds are an essential ingredient to obtain the observed mass–metallicity relation in galaxies.

Summarizing, observations provide strong evidence for the presence of galactic winds in star-forming galaxies, but the parameters of such winds are currently not tightly constrained. Models that make recourse to such winds to quench star formation require relatively high values of the wind's mass loading,  $\beta \sim 1$  for MW-like galaxies, with  $\beta$  increasing for lower mass galaxies. Moreover, do SNe-driven winds indeed meet these requirements, and if they do, why?

## 2.2 Resolving SNe in the ISM

Ideally one would wish to probe the efficiency with which star formation can drive winds with simulations that self-consistently included all the relevant physics, i.e. a full galaxy containing a star-forming ISM, those stars subsequently redistributing their energy as type II SNe explosions, including outflows and cosmological infall. Unfortunately, the range of scales involved in this problem makes such an approach currently computationally infeasible. To progress we must either truncate our resolution at some scale before we have

fully resolved the physics, or to truncate our physics such that the available resolution becomes sufficient. The former route is one where we assume that we understand the physical processes to a certain degree and make our best effort at the calculation, forcing us to go deeply into convergence studies. The latter is that of the numerical experiment where it is assumed that a certain amount of numerical calculation is possible and we make our best effort to include the processes, requiring us to make full comparison with the real Universe to test these assumptions (many simulations are, of course, a mixture of these approaches). Our focus will be on the latter case, that of the numerical experiment. We will also restrict ourselves to looking at the *launch* region of the galactic wind, where gas is expelled from the galaxy but not necessarily from the halo. This is consistent with what is needed to improve subgrid models in semi-analytic models and hydro simulations.

The motivation for our choice of scale relates to the need to resolve individual SN blast waves as they sweep the ISM (e.g. as described by Cox 1972). Briefly, such explosions involve three distinct stages (e.g. Truelove & McKee 1999), beginning with the very early stage during which SNe ejecta expand almost freely into the ISM. As the ejecta sweep-up ISM preceded by a shock, eventually a reverse shock will run back into the ejecta, heating them to very high temperatures, signalling the start of the Sedov–Taylor stage (Taylor 1950; Sedov 1959). In both stages radiative cooling is negligible and consequently they can be described by similarity solutions, but the transition between them cannot. Finally at late times, the hot interior of shocked ejecta cools radiatively, and the swept-up shell of ISM and ejecta continue to ‘snowplough’ further into the ISM, conserving momentum. Thornton et al. (1998) examine these last two states using a set of 1D simulations of the evolution of explosions in a uniform ISM, examining in detail the transition from the Sedov–Taylor phase to the snowplough phase. They claim that radiative cooling is efficient enough that typically only 10 per cent of the initial blast energy is transferred to the ISM. Notably, the amount of gas heated by these explosions is not a linear function of the SN energy, indeed it is sublinear, and thus we may expect that aggregating the energy injection of many SNe into a single event will underestimate the amount of gas heated.

We would in principle like to resolve the earliest phase of the explosions when ejecta dominate, but in this paper we restrict ourselves to initiate our SNe in the Sedov–Taylor phase. The transition between ejecta-dominated and Sedov–Taylor phase occurs approximately when the shock has swept up an amount of ISM mass that is comparable to that originally ejected. In low-density regions the size of the bubble where the transition happens may then be relatively large, and it would be worthwhile investigating whether this matters; we intend to do so in future work. Given this limitation, and for the typical ISM densities near the centre of the disc in our simulations, it then suffices to resolve scales of the order of a few parsecs to fully capture the cooling of the swept-up shell of ISM (e.g. Cox 1972), and such a simulation will be able to resolve both the cooling and some part of the adiabatic phase of the remnant.

As such the dependence of our question upon subpc phenomena can be seen only in two key areas, raising the following questions.

(i) Star formation occurs on these scales, and thus controls the distribution (in time and space) of SNe. Does this affect the properties of the galactic wind, for example because SNe explode in high-density environments and/or near to other SNe?

(ii) The medium that the SNe drive into contains structures on subpc scales, for example cores of molecular clouds. Does this departure from a classical fluid affect the large-scale wind?

We will argue that the answers to both the above questions may indeed be negative, motivating a set of simulations of a highly simplified ISM. Such a simulation would also improve our physical understanding of the role of the individual processes.

In the first question, we note that the progenitors of type II core-collapse SNe are massive stars (Smartt 2009) with lifetimes  $\sim 1\text{--}30$  Myr (Portinari, Chiosi & Bressan 1998); therefore, the majority of SN energy associated with an instantaneous burst of stars with for example a Chabrier (2003) initial mass function will be released within  $\sim 30$  Myr. It is thought that the birth cloud of such stars is likely destroyed before by the combined effects of stellar winds, protostellar jets and radiation (e.g. Matzner 2002), and there is observational evidence for this (e.g. Lopez et al. 2011). Some clouds may form by turbulent compression when overrun by a spiral arm, and may disperse by the same flows that created them in the first place on a short time-scale (Dobbs 2008, see also Tasker & Tan 2009).

In any case, when the SN explodes it will in general not do so inside its natal cloud. For this reason, we assume that the SNe explode in typical environments in the disc plane of galaxies. Note however that the SNe may still be clustered rather than Poisson, a complication that we neglect. Typical giant molecular clouds have a velocity dispersion of  $\sim 4\text{ km s}^{-1}$  (McCrack & Kafatos 1987; Scoville & Sanders 1987), which over 10 Myr results in a dispersion of around 40 pc, which is a significant fraction of our box size and the typical distance between molecular clouds.

The second question is delicate, and worthy of significant discussion. We first note that we follow the nomenclature of Wolfire et al. (1995), where the  $T \sim 100$  K phase of the ISM is called the cold neutral medium (CNM), the  $T \sim 10^4$  K phase as the warm neutral medium (WNM) and the  $T \gtrsim 10^6$  K phase as the hot ionized medium (HIM). The CNM exists in the form of dense clouds, occupying a very small fraction of the total volume but with a significant fraction of the total mass. These clouds are believed to be in pressure equilibrium (Spitzer 1956) with the WNM and HIM, thus making their energy budget (pressure  $\times$  volume) also a small fraction of the ISM thermal energy. Their pressure support is probably composed of a combination of magnetic, thermal and cosmic ray components. The proportions of energy in thermal, bulk and turbulent motions of the HIM and WNM are still not entirely known though there is consensus that much of the turbulence is supersonic (Elmegreen & Scalo 2004). A supersonic nature of turbulence in the ISM requires that the energy budget is dominated by inertial terms of the turbulent motions over the thermal and magnetic terms in the WNM and HIM.

Despite their small fraction of the energy budget, however, the cold phase can perform the role of a heat sink. Thermal energy from the warm and hot phases can be transported into the cold phase via thermal conduction which can be dissipated via the molecular transitions of this cold gas (particularly CO, H<sub>2</sub>), metal lines (in particular C I\*) and dust. The excited states of the molecules, however, are rather long lived and whilst they are certainly important for star formation they may not significantly cool the WNM phase of the ISM due to its sparse nature (de Jong, Boland & Dalgarno 1980; Martin, Schwarz & Mandy 1996). The molecules also play an important role as an absorber of photoionizing radiation; however, we will ignore radiative driving here. The simulations described in this paper simply neglect the cold phase, by truncating the cooling function below a value of  $T_0 = 10^4$  K. If we were to include cooling below  $T_0$ , we would have to include significantly more physics (magnetic fields, heat conduction, diffuse heating); here, we want



to investigate and understand the simpler yet still complex case of a two-phase medium.

We have also intentionally left out the physics of cosmic rays (see e.g. Pfrommer et al. 2007) and magnetic fields (e.g. Breitschwerdt & de Avillez 2007) which may be important in providing support against collapse, particularly in the CNM. Our goal is to understand the resultant ISM without these complications, before discussing the implications of their addition. We would also like to stress that although we have included gravity, we have not included *self*-gravity (i.e. our gravity is time-independent and only self-consistent for the initial set-up) which would be a poor approximation if we had included the dense, cold material of the CNM. Without the CNM gravity does not influence material on scales below the Jeans length of the WNM, equivalent to the scale height of the warm disc.

### 3 SIMULATION SET-UP

In the following section, we will describe the simulations we have performed of SN-driven outflows from an idealized ISM. Our simulations model the ISM and halo of a disc galaxy in a tall column, with long ( $z$ ) axis perpendicular to the galactic disc, and corotating with the disc material. We use outflow conditions at the top and bottom of the column, and periodic boundary conditions in  $x$  and  $y$ . We describe the initial conditions of the gas and the physical processes (gravity, cooling and SN feedback) we have included, and detail their numerical implementation. Finally, we describe some tests we have performed on the code and the parameters we chose to explore in our simulation set.

The simulations use a modified version of the `FLASH` 3 code (Fryxell et al. 2000). `FLASH` 3 is a parallel, block-structured, uniform time-step, adaptive mesh refinement (AMR) code. Its second-order (in space and time) scheme uses a piecewise-parabolic reconstruction in cells. Due to the extremely turbulent nature of the ISM in our simulations, we find that `FLASH` attempts to refine (i.e. to use the highest resolution allowed) almost everywhere within our simulation volume. Therefore, we disable the AMR capability of `FLASH` and run it at a constant refinement level (albeit varied for our resolution studies). To mitigate the overhead of the guard-cell calculations, we increase our block size to  $32^3$  cells per block.

For the gas physics we have assumed a monatomic ideal gas equation of state,

$$p = (\gamma - 1)\rho u, \quad (6)$$

where  $u$  is the specific thermal energy and  $\gamma = 5/3$  is the adiabatic index. This deviates slightly from the physical equation of state which should include the transition in mean particle mass that occurs as the atomic hydrogen becomes ionized, but the impact of this simplification is small compared to the other uncertainties in this kind of simulation.

#### 3.1 Physical processes

The simplified ISM discussed in Section 2.2 is shaped by three fundamental processes: gravity, cooling and energy injection from SNe, which dominate when we are only considering the WNM and HIM. We stress that our aim is to simplify the problem as much as possible so that we can extract the physical principles. In future works, we will experiment with making some assumptions more realistic. Below we discuss the effects and implementation of all these processes.

##### 3.1.1 Gravity

The gas in our simulations is initially in (vertical) hydrostatic equilibrium. In a disc galaxy the gravitational acceleration is induced by the gas and stars in the disc, baryons in the bulge and dark matter (in the halo and possibly the disc, see e.g. Read et al. 2008). Despite these complications, when one moves to the (non-inertial) frame moving locally with the disc, the dominant effective potential lies in the vertical direction, with a scale height of a few hundreds of parsecs. Since the shape of this profile is approximately in accordance with the gaseous one, we model the total gravity of all components (gas, stars, dark matter) as being in proportion to the gaseous component, with a multiplier of the inverse of the gas fraction,  $1/f_g$ , to account for the stellar and dark matter components, i.e. the gravitational potential depends on the gas density through Poisson's equation as

$$f_g \nabla^2 \phi = 4\pi G \rho. \quad (7)$$

We also make a second assumption, namely that the gravitational profile of the disc is fixed in time,  $\phi = \phi[\rho_0]$ . This is assumed because the minimum temperature of our cooling function (discussed in Section 3.1.2) sets the Jeans length of the order of the scale of the disc height, so we do not expect smaller self-gravitating clouds to appear in our simulations. In contrast, in the ISM of the MW small self-gravitating clouds can form, because the ISM does cool to lower temperatures; however, the physics of star formation is not the process we wish to address in this paper.

Other terms we have neglected include those introduced by the Coriolis force across our simulation volume, due to our non-inertial choice of frame,

$$\dot{\mathbf{v}}_{\text{cor}} = -2\boldsymbol{\Omega} \wedge \mathbf{v}, \quad (8)$$

where  $\boldsymbol{\Omega}$  is the angular velocity of the galaxy. Our simulations, however, will typically be of such short time-scales and volumes that the Rossby number (the ratio of inertial to Coriolis terms) is large. Nevertheless, more complete simulations would include this, along with the time-dependent gravitational changes introduced by spiral density waves. Note that our simulations also neglect the velocity shear that is present in a differentially rotating disc.

##### 3.1.2 Radiative cooling

The cooling function  $\Lambda(T)$  of  $T \sim 10^4 - 10^7$  K gas with solar abundances is primarily due to bound-bound and bound-free transitions of ions, whereas above  $T = 10^7$  K it is largely dominated by bremsstrahlung (Sutherland & Dopita 1993). Below  $T \sim 8000$  K there is a sharp decrease by several orders of magnitude, causing a build up of gas in the WNM. Cooling below 8000 K is due to dust, metal transition lines such as C I\*, and at very low temperatures, molecules.

Whilst the imprint of small features in the cooling function should be observable in the ISM, it is really the cut-off at  $T \sim 8000$  K that controls the WNM, and as such we approximate the cooling function with a Heaviside function with a step at  $T_0 = 10^4$  K,

$$\rho \dot{u} = \begin{cases} -\Lambda n^2, & T \geq T_0 \\ 0, & T < T_0, \end{cases} \quad (9)$$

where we in addition assume pure hydrogen gas so that the number density  $n = \rho/m_p$  and  $\Lambda = 10^{-22}$  erg cm<sup>3</sup> s<sup>-1</sup> (although it is varied in few of the simulations). We implement this very simple functional form so that we can explicitly check the effect of the normalization

of the cooling function, and to make sure that any characteristic temperature of the gas is not due to features in  $\Lambda$ .

The cooling function of equation (9) results in a cooling time for gas with  $T \geq T_0$  of

$$t_{\text{cool}} \equiv \frac{m_p u}{\Lambda n} \approx 660 \text{ yr} \left( \frac{T}{T_0} \right) \left( \frac{n}{1 \text{ cm}^{-3}} \right)^{-1} \times \left( \frac{\Lambda}{10^{-22} \text{ erg cm}^3 \text{ s}^{-1}} \right)^{-1}. \quad (10)$$

Since we have chosen a discontinuous function for our cooling, we implement a scheme in our code which prevents cooling below  $T_0$  (although the hydrodynamic forces can still achieve lower temperatures adiabatically). This largely prevents the overshoot errors resulting from an explicit solver in this kind of problem.

To test the importance of the choice of cooling function, we also implemented the cooling function appropriate for cosmic gas with solar abundance pattern from Sutherland & Dopita (1993),

$$\Lambda_{\text{SD}}(T) = 5.3 \times 10^{-24} \left( T_8^{1/2} + 0.5 f_m T_8^{-1/2} \right) \text{ erg cm}^3 \text{ s}^{-1}, \quad (11)$$

where  $T_8 \equiv T/10^8 \text{ K}$ , with  $f_m = 0.03$  for low-metallicity gas and  $\Lambda = 0$  for  $T < 10^4 \text{ K}$ . All runs where this cooling function is used are marked ‘SD’ (see Table 1). The minimum of this cooling function is at  $5 \times 10^7 f_m \text{ K}$ , where the cooling rate

$$\Lambda_{\text{SD,min}} = 1.30 \times 10^{-24} \text{ erg cm}^3 \text{ s}^{-1} \quad (12)$$

(ignoring the cut-off below  $10^4 \text{ K}$ ). In Appendix A, we show that the behaviour of the ISM in our simulations is surprisingly independent of the exact shape of the cooling function  $\Lambda(T)$ , although it depends on the minimum value at high temperatures  $\gg 10^4 \text{ K}$ .

### 3.1.3 Energy injection by supernovae

The Kennicutt–Schmidt (KS) relation connects the observed surface density of star formation in a disc galaxy,  $\dot{\Sigma}_*$ , to its gas surface density  $\Sigma_g$ ,

$$\dot{\Sigma}_* \approx 2.5 \times 10^{-4} \Sigma_{\text{gl}}^{1.4} \text{ M}_{\odot} \text{ yr}^{-1} \text{ kpc}^{-2} \quad (13)$$

(Kennicutt 1998), where  $\Sigma_{\text{gl}} \equiv \Sigma_g / 1 \text{ M}_{\odot} \text{ pc}^{-2}$ . We also perform some simulations with an alternative formulation using a higher star formation rate, more commonly used in cosmological simulations,

**Table 1.** Parameter variations in our simulation. Each simulation is initialized with an isothermal profile with a surface density of  $\Sigma_g$  in cold gas and gas fraction of  $f_g$  (i.e. a total mass density of  $\Sigma = \Sigma_g / f_g$ ). Star formation proceeds either in a pure KS prescription or the dynamical time variation in equation (A1). Cooling above  $10^4 \text{ K}$  proceeds at a rate  $\Lambda$  and we study the simulations at several resolutions to test for convergence.

	Range of values explored	Fiducial value
$\Sigma_g (\text{M}_{\odot} \text{ pc}^{-2})$	2.5, 3.23, 4.17, 5.39, 6.96, 8.99, 11.61, 15, 30, 50, 150, 500	11.61
$f_g$	0.01, 0.015, 0.022, 0.033, 0.050, 0.1, 0.2, 0.5, 1.0	0.1
$\dot{\Sigma}_*$	Equations (13) and (A1)	Equation (13)
$\Lambda (\text{erg cm}^3 \text{ s}^{-1})$	1, 2, 4, 8, $16 \times 10^{-22}$ , SD	$10^{-22}$
Resolution (pc)	0.78, 1.56, 3.12, 6.25	–

discussed in Appendix A. Notably this introduces an additional dependence on the gas fraction of the disc,  $f_g$ , that is absent from the KS relation. Our idealized model of an SN explosion is the injection of  $10^{51} \text{ erg}$  (Cox 1972) of thermal energy in a small volume, implicitly assuming instantaneous thermalization of the SN ejecta. The distribution in time of these is taken to be a Poisson process (the Poisson process has the Markov property and so our SNe are independent) with a time-independent rate computed from the initial parameters of the disc. For the local spatial distribution of SNe, we assume the star formation rate to be proportional to the initial density, i.e.

$$\mathbb{E}[\dot{\rho}_* dV dt] = \dot{\Sigma}_* \frac{\rho(t=0)}{\Sigma_g} dV dt. \quad (14)$$

A consequence of this choice is that if the scale height of the gas profile evolves significantly the distribution of SNe will become inconsistent with the instantaneous mass profile. We discuss this further later.

Given the star formation rate, the associated core-collapse SN rate is computed assuming the stellar initial mass function yields  $\varepsilon_{100}$  SNe per  $100 \text{ M}_{\odot}$  of star formation. For reference, for a Chabrier (2003) initial mass function with stars with masses  $\in [0.1, 100] \text{ M}_{\odot}$ , of which those with mass in the range  $[6, 100] \text{ M}_{\odot}$  undergo core collapse,  $\varepsilon_{100} = 1.8$ .

The final element of the SN prescription is the distribution of the injected energy over the computational grid. The choice of volume over which to spread the thermal energy of the SNe is influenced by two considerations. If the volume is too large, the remnant will evade the adiabatic expansion phase and immediately proceed to the radiative phase (Cox 1972; Creasey et al. 2011). If the volume is very small, the code will require many extra time steps evaluating the initial stages of an ST blast wave and will perform unnecessary computation.<sup>1</sup> Following Cox (1972), the radius at which the blast wave cools and forms a dense shell is

$$R_s = 15.6 \left( \frac{E_{\text{SN}}}{10^{51} \text{ erg}} \right)^{3/11} \left( \frac{\Lambda}{10^{-22} \text{ erg cm}^3 \text{ s}^{-1}} \right)^{-2/11} \times \left( \frac{n}{1 \text{ cm}^{-3}} \right)^{-5/11} \text{ pc}; \quad (15)$$

however, to account for higher densities and the numerical spreading of shocks it is wise to resolve a fraction of this (Creasey et al. 2011).

Taking the above into consideration, for our simulations we spread the thermal energy of each SN over several cells given by the multivariate (3D) normal distribution of standard deviation 2 pc, consistent with being smaller than the cooling radius of equation (15) for densities  $n < 77 \text{ cm}^{-3}$  ( $\rho < 1.3 \times 10^{-22} \text{ g cm}^{-3}$ ).

### 3.1.4 Time-stepping

In addition to the numerical considerations described above, we also needed to make some adjustments to the time-step calculation in FLASH. The default time-stepping scheme in FLASH uses a Strang-split method (Strang 1968, an operator splitting method where the hydrodynamic update occurs in two half steps, with the order in which the Riemann solver operates reversed from  $xyz$  to  $zyx$  between the first and the second half step). Source terms, such as the

<sup>1</sup> To get some idea of the computational requirement of this, we recall that the velocity of a 3D Sedov blast wave evolves as  $v \sim t^{-3/5}$ . Substituting this into the Courant–Friedrichs–Lewy (CFL) condition, we see that the number of time steps required to reach a given radius is proportional to that radius.

injection of SN energy, are evaluated at the end of each half step, after the Riemann solver has been applied. This makes the implementation of the SN energy injection problematic, as the thermal energy in a cell can increase by many orders of magnitude followed by a hydrodynamic step before a new time step is calculated. The latter hydrodynamic step then almost inevitably violates the CFL condition and the Riemann solver fails to converge. We avoid this by making the time-step limiter for the SN source terms *predictive*, i.e. we utilize the foreknowledge of the pre-computed SN times to recognize when an SN will occur before the end of the time step given by the CFL condition and return a time step of either up to just before the SN or of the predicted CFL time step after the SN has occurred, whichever is smaller.

It is worth contrasting this with some other simulations of the ISM. In a series of simulations, de Avillez & Breitschwerdt (2004, 2005a,b) use a set-up similar to that of ours, with imposed gravity, cooling, SNe turbulence and magnetic fields in columns through discs of  $1 \times 1 \times 10 \text{ kpc}^3$ , although the focus is not on the mass loading. More recently, the ERIS simulations (Powell et al. 2011) simulated the ISM in a single high-redshift dwarf galaxy. Cooper et al. (2008) perform a simulation of the central region of an M82-like starburst galaxy with gravity, cooling and energy injection due to SNe (although this energy injection is continuous within a central volume, rather than stochastic as in our simulations).

### 3.1.5 Code tests

A set-up as complex as this requires some testing to confirm that the physical processes have been correctly implemented. As such we ran a number of simpler problems as well as the convergence tests in Appendix A.

In order to test our hydrostatic set-up, we simulated the disc without SNe for several dynamical times. Some sub-per cent evolution in the gas occurred, almost certainly due to our evaluation of the analytic solution for the gravitational potential and density at the centres of cells producing some discretization error. The implementation of the cooling function was tested largely in Creasey et al. (2011). We follow a similar approach where we made the cooling rate for each cell an output of our code which was compared with the instantaneous rate predicted from the temperature and density of each cell (again there were small differences due to the comparison of an instantaneous rate with the average from an implicit scheme).

The implementation of the individual SN in our set-up is largely similar to that of the ST blast wave solution implemented in FLASH as a standard test, and we compared it to the similarity solution. We calculate the location and times of SN explosions ahead of the simulation, and verify that the code indeed injects them correctly.

We initially also performed these calculations using the GADGET simulation code (Springel 2005) that has been successfully applied to many cosmological simulations. Unfortunately, the adaptive time-stepping algorithm proved problematic for correctly following the blast waves, and we noticed similar problems as recently highlighted by Durier & Dalla Vecchia (2012); particles may be on long time steps in the cold ISM, and largely fail to properly account for being shocked by the blast wave from a nearby particle. Durier & Dalla Vecchia (2012) addressed this problem with a time-step propagation algorithm; however, we did not have this or the algorithm of Saitoh & Makino (2009) available and the alternative of a global time step would have been far too computationally expensive due to the large dynamic range in time steps required

in the evolution of the blasts. As such we used the global adaptive time-stepping algorithm of FLASH.

### 3.2 Initial conditions

Our initial set-up is a tall box poking vertically through an idealized disc profile. We choose the long axis in the  $z$ -direction in order to capture a multiple of the gravitational scale height of the disc. The profile is a 1D gravitationally bound isothermal one with gas surface density  $\Sigma_g$ . As discussed in Section 3.1, we have excluded the effects of shear (due to the Coriolis force in the disc) and large-scale motions which may drive some turbulence down to the small scales. The gas density is

$$\rho(z) = \frac{\Sigma_g}{2b} \text{sech}^2\left(\frac{z}{b}\right), \quad (16)$$

and the corresponding gravitational acceleration follows from equation (7),

$$\nabla\Phi = 2\pi G \Sigma_g f_g^{-1} \tanh\left(\frac{z}{b}\right). \quad (17)$$

Setting the gas temperature to  $T_0$  (which is also the base of the imposed cooling function) and assuming the gas to be initially in hydrostatic equilibrium, the scale height is

$$b = \frac{f_g k_B T_0}{m_p \pi G \Sigma_g} \approx 61 \left(\frac{f_g}{0.1}\right) \left(\frac{\Sigma_g}{10 \text{ M}_\odot \text{ pc}^{-2}}\right)^{-1} \text{ pc}, \quad (18)$$

where numerically

$$\rho(z) \approx 3.4 \left(\frac{\Sigma_g}{10 \text{ M}_\odot \text{ pc}^{-2}}\right)^2 \left(\frac{f_g}{0.1}\right)^{-1} \text{sech}^2\left(\frac{z}{b}\right) m_p \text{ cm}^{-3}. \quad (19)$$

The (vertical) dynamical time of the disc is

$$t_{\text{dyn}} = \sqrt{\frac{b f_g}{G \Sigma_g}} \approx 12 \times 10^6 \left(\frac{f_g}{0.1}\right) \left(\frac{\Sigma_g}{10 \text{ M}_\odot \text{ pc}^{-2}}\right)^{-1} \text{ yr}, \quad (20)$$

and the ratio of the dynamical time to the cooling time is

$$\zeta \equiv \frac{t_{\text{dyn}}}{t_{\text{cool}}} \approx 1.7 \times 10^5 \left(\frac{\Lambda}{10^{-22} \text{ erg cm}^3 \text{ s}^{-1}}\right) \left(\frac{\Sigma_g}{10 \text{ M}_\odot \text{ pc}^{-2}}\right). \quad (21)$$

The exact gravitational potential is given by

$$\Phi(z) = 2\pi G b \Sigma_g f_g^{-1} \log \cosh\left(\frac{z}{b}\right), \quad (22)$$

and the pressure in hydrostatic equilibrium is

$$p = \pi G \Sigma_g f_g^{-1} b \rho(z) \approx 3.3 \times 10^4 \left(\frac{\Sigma_g}{10 \text{ M}_\odot \text{ pc}^{-2}}\right)^2 \times \left(\frac{f_g}{0.1}\right)^{-1} \text{sech}^2\left(\frac{z}{b}\right) \text{ K cm}^{-3}. \quad (23)$$

Finally, the hydrostatic temperature for all our discs is chosen to be

$$T_0 = 10^4 \text{ K}. \quad (24)$$

### 3.3 Numerical parameters and boundary conditions

To produce simulations of a realistic ISM, we make the following choices of parameters. In terms of resolution we must have cell sizes fine enough to capture the cooling of SN remnants (equation 15), yet the simulation volume needs to be large enough to capture several scale heights of the star-forming disc. In terms of gas fractions and gas surface densities, we choose values approximating those in the solar neighbourhood and some variations. In practise we chose fiducial values for the disc parameters ( $\Sigma_g = 11.61 \text{ M}_\odot \text{ pc}^{-2}$ ,  $f_g = 0.1$ ) and examine this reference model in detail. For reference, the gas surface density of the solar neighbourhood of the MW has been estimated at  $\Sigma_g = 13.2 \text{ M}_\odot \text{ pc}^{-2}$ , with a dynamical density of  $\Sigma_* = 74 \text{ M}_\odot \text{ pc}^{-2}$  (Flynn et al. 2006).

In order to test the dependence of winds on the disc properties, we perform a slice of the parameter space varying  $\Sigma_g$  and  $f_g$  (see Table 1). Not all parameter combinations are explored, as we cut out the simulations with very small scale heights (due to resolution constraints) and large-scale heights (due to the finite box size). The dependence of the results on cooling, resolution, box size, star formation rate and run time can be seen in Appendix A.

All our simulations were conducted in box sizes of  $200 \times 200 \times 1000 \text{ pc}^3$  with constant cell sizes. All cells were cubic, and in the vertical direction the number of cells for our default resolution is 640, with the corresponding cell size of 1.6 pc. We vary the numerical resolution using 160, 320, 640 and 1280 cells in  $z$ , with the corresponding cell sizes ranging from 6.25 to 0.78 pc. These simulations are denoted L2, L3, L4 and L5, respectively. We also test the effect of adjusting our box size with simulations of two and four times the width (see Appendix A).

The gas surface density  $\Sigma_g$  is varied from 2.5 to  $15 \text{ M}_\odot \text{ pc}^{-2}$  in eight logarithmically spaced steps followed by three additional steps of 30, 50 and  $500 \text{ M}_\odot \text{ pc}^{-2}$ . Notably some of these are below the minimum surface density threshold for star formation of Schaye (2004) of  $3\text{--}10 \text{ M}_\odot \text{ pc}^{-2}$  (although there is evidence that star formation proceeds below this level, e.g. Bigiel et al. 2008). The gas fraction  $f_g$  was varied from 0.01 to 0.05 in five logarithmic steps followed by additional steps of 0.1, 0.2, 0.5 and 1.0. The cooling function  $\Lambda$  was varied from  $3.9 \times 10^{-25}$  to  $1.6 \times 10^{-21} \text{ erg cm}^3 \text{ s}^{-2}$ , and we ran additional models with the Sutherland & Dopita (1993) cooling function as parametrized in equation (11). Each of our experiments is evolved over 20 Myr (typically thousands of cooling times) in order to simulate many SNe.

## 4 RESULTS

In this section, we discuss the results of the simulations described in the previous section. We begin with a discussion of a single snapshot, allowing us to investigate the instantaneous properties of the idealized ISM and outflow. We then move to looking at the evolution of a simulation and the statistics we can measure before finally investigating the effects of all the parameters discussed in the previous section.

### 4.1 Fiducial run

The impact of SNe depends strongly on whether they explode in the dense gas or in the more rarefied HIM. The SNe in the disc blast bubble in the ISM and compress the warm gas into thin sheets and clouds. We note that between the different simulations the volume of the warm medium can vary from a series of disconnected, nearly spherical regions to a highly porous stratus that approximately covers the base of the disc potential. We will use the term ‘clouds’ to apply to both. When SNe explode in the rarefied regions, either at the edge of the disc or inside previously evacuated bubbles, the heated gas pushes out of the central region and then rapidly escapes from the simulation volume in a zone of acceleration above and below the disc. This is the ISM portion of the galactic wind (i.e. the gas whose thermal energy far exceeds the potential barrier to escaping the disc). Some warm clouds are dragged along with this wind. A movie of this simulation is available online along with time-dependent versions of some of the other figures.<sup>2</sup>

In Fig. 1 we show an  $x$ – $z$  slice of the fiducial run, at a time of 12 Myr. We can see that the combined action of multiple SNe has disrupted the disc considerably, with the warm gas squeezed into dense sheets and globules entrained in outflowing gas, and around half the volume now occupied by a hot tenuous phase. The gas appears to be in well-defined phases, an HIM (greens and yellows) and a WNM (dark blue) with little gas at intermediate temperatures (see also Fig. 2). Notably there is more temperature variation in the hot phase (a few orders of magnitude) than in the WNM (which is all close to  $10^4 \text{ K}$ ). The density plot also appears to show two distinct phases, a high- and low-density medium, where the high densities show up in the temperature plots as WNM. In the velocity plot we can see a bulk vertical outflow from the disc, with velocity correlating with height. The pressure plot shows a dramatically lower dynamic range than either the temperature or density plots, but has some distinctive shells due to individual SN remnants. The impression of a volume in quasi-pressure equilibrium is reinforced by the profile plot where the temperature and density fluctuations appear to anti-correlate, resulting in comparatively small pressure variations.

Above the plane of the disc the outflow is also very inhomogeneous, containing significant turbulence as well as some warm clouds or globules with cometary shapes. The corresponding locations in the density and pressure panels reveal that these clouds are also overdense and slightly underpressured. In velocity the clouds appear to be receding from the disc at a lower velocity than the HIM, that is rushing past them at around  $100 \text{ km s}^{-1}$ . The hot wind is stripping the edges of these warm clouds, as evidenced by their tails (see also the movie online).

After only 12 Myr, the original disc has undergone considerable disruption but is still observed as a connected feature in this slice (and the majority of the mass of the simulation remains in the central region). The disc has also been disrupted asymmetrically, with more mass pushed into the lower half space by the stochastic locations of the SNe. The externally imposed gravity will ultimately return this mass to the base of the potential, yet the combined action of the SNe has been enough to displace it.

Whilst we have run these simulations at different resolutions, it is important to note that the turbulent and chaotic nature of these simulations results in specific features such as individual clouds being at different locations or indeed absent between the different

<sup>2</sup> See <http://astro.dur.ac.uk/~rmdq85/>



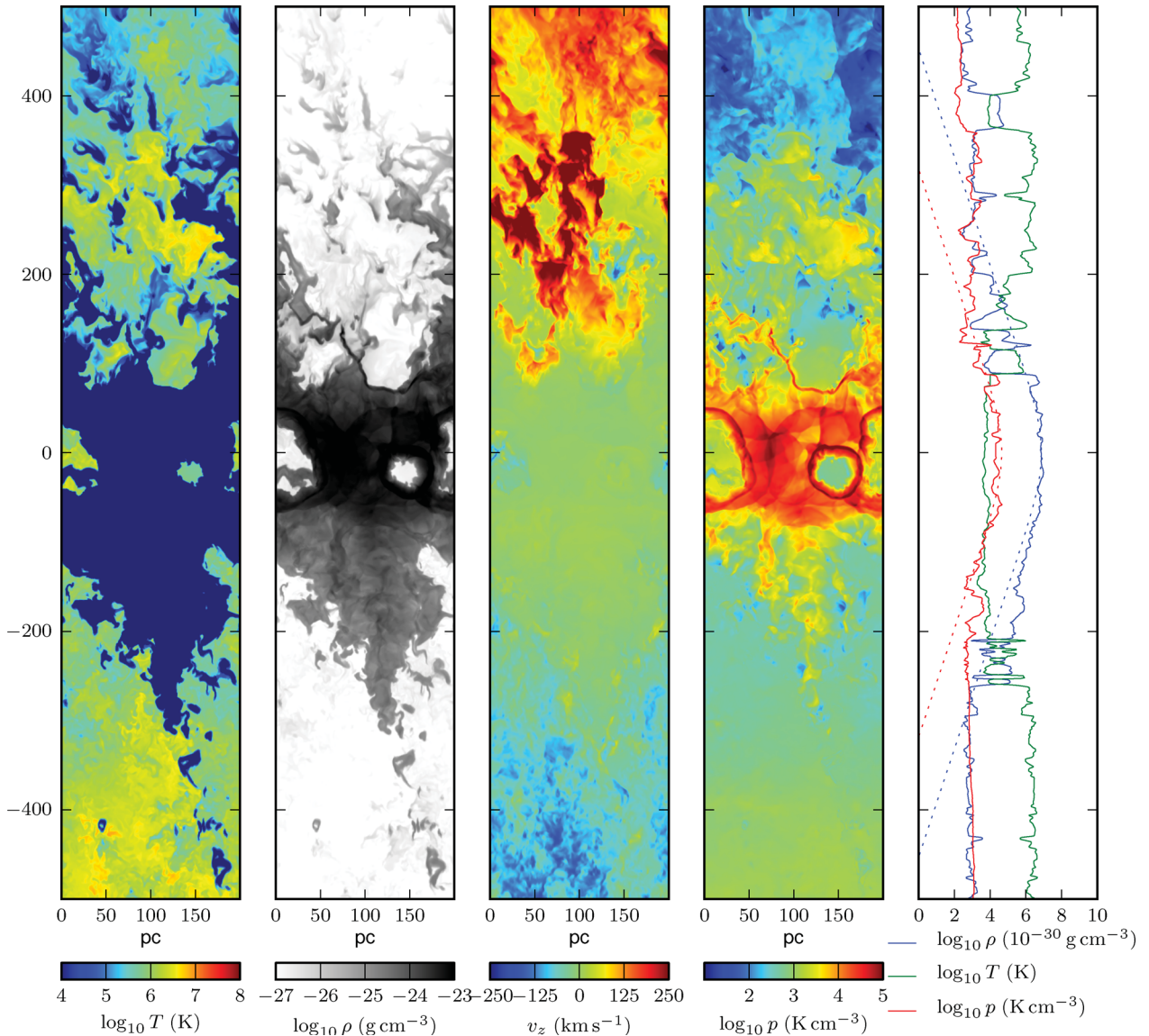


**Figure 1.** Left to right: temperature, density, vertical velocity and pressure plots through a slice of the simulation, at time 5 Myr. Temperature is coloured between  $10^4$  and  $10^8$  K, density between  $10^{-27}$  and  $10^{-23}$   $\text{g cm}^{-3}$ ,  $v_z$  from  $-250$  to  $250$   $\text{km s}^{-1}$  and pressure from  $10$  to  $10^5$   $\text{K cm}^{-3}$ . On the far right is the profile of density, temperature and pressure along a vertical line through the centre of the slice. In dotted blue and red we show the hydrostatic density and pressure profiles at  $t = 0$ . Around  $z = 0$  we can see the disrupted disc in the temperature and density plots, with the warm gas squeezed into sheets and globules, and a significant fraction of the volume now consumed by a hot ( $\sim 10^{6.5}$  K) sparse phase. In the velocity plot, we can see a bulk vertical outflow from the disc. The outflow is inhomogeneous, entraining significant turbulence as well as some warm gas, swept away from the disc.

runs. Global properties, however, such as the outflow mass and temperature will be less stochastic, and we devote Appendix A to the convergence study of these properties. In general, these simulations are numerically well converged. In the following figures, we also include a few convergence comparisons where space allows.

The values of the ISM pressures in our simulations are around  $10^3$   $\text{K cm}^{-3}$ , comparable to the pressure in simulations such as that of Joung & Mac Low (2006) and Joung et al. (2009). Estimates of the pressure of a star-forming ISM vary, Bowyer et al. (1995) find a pressure of around  $2 \times 10^4$   $\text{K cm}^{-3}$  in the local bubble, although in the centre of the highly star-forming region of 30 Doradus, Lopez et al. (2011) estimate a pressure of  $\sim 7 \times 10^6$   $\text{K cm}^{-3}$  from infrared dust measurements.

Fig. 1 suggests that the hot and warm phases are quite distinct, and we test this by inspecting the volume fractions in Fig. 2. The warm

phase is very tightly distributed below  $10^4$  K, as we might expect since the only mechanism for cooling here is by adiabatic expansion. The lack of intermediate temperatures suggests that they have very short cooling times, which is consistent with a pressure equilibrium view. The hot tail of the distribution suggests that the hottest gas either mixes with cooler gas or escapes from the simulation volume.

Fig. 3 is the density–temperature phase diagram for the fiducial model at L3 resolution (3 pc cells), which is broadly described by two regions. In the lower right, lying horizontally at a nearly constant temperature of the order of  $T_0 = 10^4$  K (the base of the cooling curve) is the WNM, which contains most of the mass. The HIM is in the upper left. On examination of the time-dependent movie of this simulation, we see that the structure in the HIM is due to multiple SNe, each SN blast forms a ‘finger’ roughly along an isobar, and as these shocked regions evolve and expand these lines

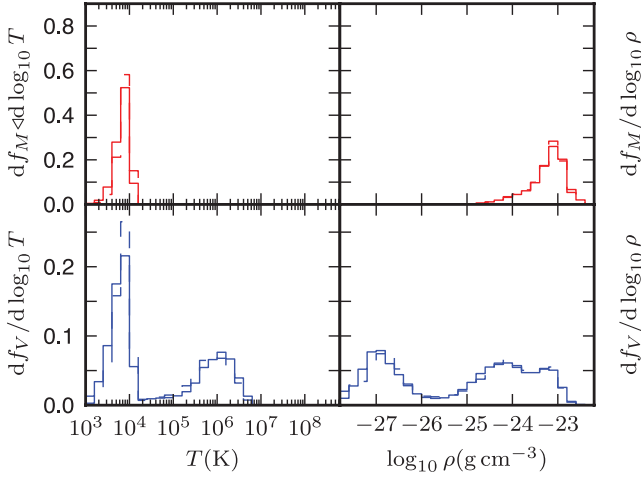


**Figure 2.** Density and temperature probability distributions for the fiducial run at 10 Myr, as shown in Fig. 1, solid, dashed and dotted lines denote the L4, L3 and L2 resolution runs, respectively. Upper panels show the mass fractions in temperature and density and lower panels show the corresponding volume fractions. We see a clear bimodality between the WIM (at low temperature and high density) and the HIM (at high temperature and low density). Almost all of the mass is in the WIM phase, but a significant fraction of the volume is in the HIM.

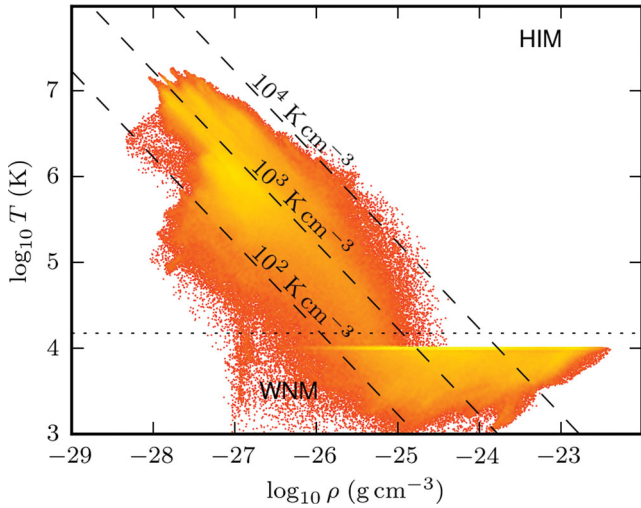


**Figure 3.** Density-temperature histogram for the fiducial model at L3 resolution. Each pixel is coloured by the fraction of cells at given  $\rho$ - $T$ . Dashed black lines indicate lines of constant pressure,  $p/k_B = 10^2, 10^3$  and  $10^4$  K cm $^{-3}$  as indicated in the panel. We see that the simulation volume is in an order of magnitude pressure equilibrium, with a bimodality in the gas phases into HIM and WIM that we have segregated approximately with the dotted black line, a temperature cut at 15 000 K. Above  $10^4$  K and  $\rho > 10^{-24}$  g cm $^{-3}$ , the cooling time of the gas is very short and the gas quickly cools to  $10^4$  K. Some gas reaches lower than this temperature due to adiabatic expansion.

descend to lower temperatures forming the mixture in the lower right-hand region. As one looks to lower temperatures the fingers start to merge and become indistinct. We see that instantaneously we have variations in pressure within approximately one order of magnitude, and that a significant fraction of the volume is in the HIM.

#### 4.1.1 The characteristic temperature of the HIM

It is interesting to consider where the characteristic temperature of the hot phase may appear from. We recall that the cooling function used in these simulations was intentionally chosen to be independent of temperature for  $T \geq T_0 = 10^4$  K, and as such cannot by itself introduce a characteristic temperature scale, yet in Fig. 2 the hot gas quite clearly has a well-defined peak temperature  $\sim 10^6$  K. This is much higher than the escape temperature for the simulation volume ( $\sim 10^5$  K, derived from equation 22), and as our SNe are injected just as thermal energy, there is no characteristic temperature for this gas. Since all of the hot gas in our simulations has been produced by the action of SNe, it is reasonable to suppose that the temperature of this phase may be determined by the transition from the adiabatic to the momentum-driven phases, as described by Cox (1972), Chevalier (1974) and Larson (1974).

In this explanation, the SNe would rapidly expand in the adiabatic phase until the action of cooling relative to expansion causes the growth of the remnant to decelerate, and the edge to form a cold dense shell. This shell still expands, but at a considerably reduced rate, driven primarily by the momentum of the shell. We expect the adiabatic phase to remain approximately spherical due to the short sound crossing time within the hot volume; however, when the blast enters the momentum-driven phase, the cooling shell is unstable and the remnant can become quite asymmetric. If the edge of the remnant reaches other sparse material, the hot interior of the remnant can leak out (i.e. a ‘chimney’ such as those seen in Ceverino & Klypin 2009), otherwise the hot material will gradually be consumed into the dense shell as it radiates away its pressure support.

The post-shock temperature,  $T_s$ , of the hot remnant at which the ‘sag’ occurs (when cooling dominates over adiabatic expansion) was calculated in Cox (1972) as

$$T_s \approx 2.0 \times 10^6 \left( \frac{n}{1 \text{ cm}^{-3}} \right)^{4/11} \left( \frac{E_{\text{SN}}}{10^{51} \text{ erg}} \right)^{2/11} \times \left( \frac{\Lambda}{10^{-22} \text{ erg cm}^3 \text{ s}^{-1}} \right)^{6/11} \text{ K}. \quad (25)$$

The obstacle which radiates away the energy of the SN is the warm disc gas of Fig. 1. Taking a mean density of these from Fig. 2

$$n = 3 \text{ cm}^{-3} \quad (26)$$

( $\rho = 5 \times 10^{-24}$  g cm $^{-3}$ ), we expect a characteristic temperature of the remnants to be  $T_{\text{hot}} \approx 3 \times 10^6$  K, very close to our HIM temperature of  $\sim 10^6$  K.

Another interesting application of equation (25) is to estimate the mass heated by a single SN before it ends the adiabatic phase. By finding the amount of mass required to absorb the thermal energy of an SN we derive

$$M_{\text{hot}} = \frac{2}{3} \frac{m_p E_{\text{SN}}}{k_B T_s} = 1350 M_{\odot} \left( \frac{T_s}{3 \times 10^6 \text{ K}} \right)^{-1} \frac{E_{\text{SN}}}{10^{51} \text{ erg}}, \quad (27)$$

where we have neglected the initial thermal energy of the heated gas, the SN ejecta themselves (see also Kahn 1975), and assumed that none of the SN energy has yet been lost radiatively. For comparison, in the model of Efstathiou (2000), an SN evaporates a similar mass  $M_{\text{ev}} \sim 540 M_{\odot}$  of cold clouds. If all this hot gas were to escape from the simulation without entraining any other material, we would

derive a mass loading of

$$\beta = \frac{M_{\text{hot}} \varepsilon_{100}}{100 M_{\odot}} \approx 13 \varepsilon_{100} \left( \frac{n}{3 \text{ cm}^{-3}} \right)^{-4/11} \left( \frac{E_{\text{SN}}}{10^{51} \text{ erg}} \right)^{9/11} \times \left( \frac{\Lambda}{10^{-22} \text{ erg cm}^3 \text{ s}^{-1}} \right)^{-6/11}, \quad (28)$$

$$\beta \approx 13 \varepsilon_{100} \left( \frac{\Sigma_g}{10 M_{\odot} \text{ pc}^{-2}} \right)^{-8/11} \left( \frac{f_g}{0.1} \right)^{4/11} \times \left( \frac{E_{\text{SN}}}{10^{51} \text{ erg}} \right)^{9/11} \left( \frac{\Lambda}{10^{-22} \text{ erg cm}^3 \text{ s}^{-1}} \right)^{-6/11}, \quad (29)$$

where in equation (28) we have used the warm cloud density  $n = 3 \text{ cm}^{-3}$  from equation (26), and in equation (29) we have used the hydrostatic mid-plane density from equation (19). The mass loading is higher at lower surface densities (and also volume densities), at higher gas fractions, and for gas that cools more slowly, and increases with the SN energy injected. If all the gas escapes at  $T = T_s$  then this is an upper bound for the mass loss, since some energy will be converted into other forms such as radiation and turbulent motion, and for this simulation we do find that the measured  $\beta$  is significantly below this (see Section 5). Notably many versions of semi-analytic models such as GALFORM assume  $\beta$  close to this maximum.

In this section, we have described a snapshot of a simulation of a patch of the ISM with similar parameters to that of the solar neighbourhood. We have reproduced a warm and hot phase in order of magnitude pressure equilibrium, with a value similar to that estimated for the local volume. We have explored the relation between the temperature of the hot phase and related this to the density of the warm phase via the energy of each SN and the cooling time of the gas.

## 4.2 Time dependence

We now turn our attention to the time dependence within our simulation. We have seen in Fig. 1 that our idealized disc is disrupted by the energy injection from SNe, and we are interested in the evolution that results from this. The injected energy can be converted into a number of forms, heating of the warm phase, the thermal energy of the hot phase, the mechanical energy of turbulence and the wind, the gravitational potential of the gas as it is lifted out of the disc, and the photons lost through radiative cooling. It is worth recalling that cooling is one of the two ways in which energy can leave the simulation volume, the second being the advection of mass across the vertical boundaries of the simulation, taking with it the thermal, mechanical and gravitational potential energy of the gas.

Fig. 4 is a ‘space–time’ plot of the onset of the outflow: time is along the horizontal axis and the projected mean temperature,  $\bar{T}$ , as a function of height is colour coded and shown on the vertical axis, red dots correspond to the times and location of individual SN injection events. In order to reduce the effects of stochastic outflows we performed this simulation in a larger box, of width 800 pc. The initially hydrostatic gas at temperature  $T = T_0$  seen at the far left of the figure is quickly replaced by gas at a range of temperatures. The dark blue coloured band, corresponding to  $\bar{T} \approx T_0$ , episodically widens as a function of time, as the disc puffs up. Gas with a mean temperature  $\bar{T} \sim 10^6 \text{ K}$  is seen to stream out of the disc at a range of velocities. From Fig. 2 we recall that there is actually very little

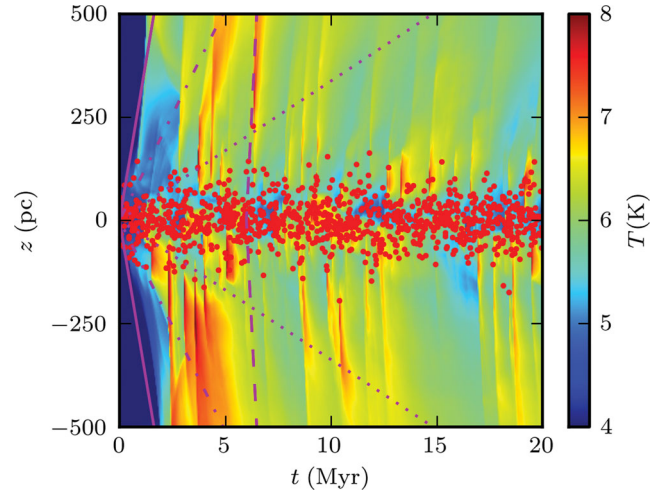


**Figure 4.** Volume-weighted mean temperature as a function of height and time, for the fiducial disc parameters yet in a wider box of  $800 \times 800 \times 1000 \text{ pc}^3$ . At each height we have taken the average over a horizontal slice. Superimposed are red dots indicating the locations and times of the SN events. As the simulation progresses, the activity of many SNe shock heat gas and drive a vertical wind from the disc at around  $300 \text{ km s}^{-1}$ . Dotted, dot-dashed, solid and dashed magenta lines denote outflows of 33, 100, 300 and  $1000 \text{ km s}^{-1}$ , respectively. Subsequent and around each SN can be seen a pulse (in orange) in the temperature. After a short ( $t < 1 \text{ Myr}$ ) flurry of SN activity within the disc ( $z = \pm 53 \text{ pc}$ ), the shocked regions begin to combine and rise out of the disc and the simulation volume. Occasionally, individual SNe high above the disc (where the gas density is low) make a significant individual contribution to the wind. The  $1000 \text{ km s}^{-1}$  line has been offset to start at 6 Myr to be compared with the propagation of one of such temperature pulses.

gas by mass at  $10^6 \text{ K}$ ; however, by volume the mean temperature will be close to this. Around each SN a plume of hot gas can be seen (cyan against the colder dark blue gas). At late times these plumes combine and drive the galactic wind.

Comparing with the velocity lines we can see the evolution of the outflow velocity with time, with many structures with velocities in the range of  $30\text{--}300 \text{ km s}^{-1}$ . Superposed, however, are some extremely steep (with respect to time, i.e. high velocity) discontinuities where much of the simulation volume rapidly experiences an increase in temperature. These appear to propagate from individual SNe, and race away from the disc with velocities in excess of  $1000 \text{ km s}^{-1}$ , consistent with a sudden pressurization of the hot phase of the ISM.<sup>3</sup> This increased pressure causes stripping from the warm material as shocks drive into the warmer region of the cloudy medium, adding to the mass of the hot phase.

To analyse our simulations we reduced our data set down to the following parameters, listed below. These are chosen to give us a broad overview of the evolution of the star-forming disc, rather than information on the individual cells and clouds. For these parameters there is some freedom of definition, e.g. when one attempts to measure the pressure one could take the mid-plane pressure, the pressure within the star-forming scale height  $b$ , the mean pressure within the simulation volume or the mean pressure within a volume adjusted by some measure of the current disc scale height. In all cases, we have attempted to choose a definition which strikes the balance between reducing stochasticity (some candidate measures

<sup>3</sup> For reference, the temperature that corresponds to a given sound speed  $c$  is  $T = 7.3 \times 10^7 \text{ K} (c/1000 \text{ km s}^{-1})^2$ .



show considerably more noise than others) and ease of physical intuition.

(i) Mass ejection,  $\Sigma_{\text{ej}}(t)$ , is the amount of gas ejected from the disc per unit area. This is calculated from the mass advected through the boundary at  $z = \pm 500$  pc, divided by the surface area of the simulated column. This quantity is used in the calculation of the cosmologically important quantity  $\beta = \dot{\Sigma}_{\text{ej}}/\dot{\Sigma}_*$  where we have identified the mass ejected from the idealized disc with the mass ejected from the galaxy. To achieve the nearest correspondence we try to maximize the volume we are measuring the loss from, i.e. the entire simulation volume. The corresponding normalized quantity is the fraction of gas remaining in the disc,  $f_{\Sigma} \equiv 1 - \Sigma_{\text{ej}}/\Sigma_g$ .

(ii) Cold/hot gas surface density is the remaining cold/hot gas surface densities in the simulation volume, and in combination with the mass ejected, sum to the initial gas surface density  $\Sigma_g$ .

(iii) Cold volume fraction,  $f_{\text{cold}}$ , is the volume fraction of cold gas, sometimes quoted in terms of the porosity

$$P = -\log f_{\text{cold}} \quad (30)$$

(Silk 2001). We distinguish between cold and hot phases at a cut-off of  $2T_0$  (i.e. twice the lower limit of our cooling function). Though the choice of  $2T_0$  may seem arbitrary, it is apparent from Fig. 2 that the bimodality of the warm and hot phases is quite strong, so the dependence of our results on the choice of temperature cut-off is rather low. Since the effectiveness of SNe in driving feedback is highly suppressed in dense (and cold) regions, the volume filling factor largely determines the probability that an individual SN will explode in the hot phase. The volume we study is  $z \in [-250, 250]$  pc, as we are not interested in the hot gas far from the plane of the disc (where SNe do not occur).

(iv) Pressure,  $p$ , is the mean pressure in the entire simulation volume. Hot material from the disc is ejected by a mean pressure gradient to the edge of the simulation volume; however, the stochastic nature of SN events creates a significant variation over small time-scales and large spatial scales<sup>4</sup> and thus it is desirable to smooth the pressure estimate over as large a volume as possible.

(v) Half-mass height,  $\lambda_{1/2}$ , is defined as the height where  $z \in [-\lambda_{1/2}, \lambda_{1/2}]$  contains half the original gas mass of the disc,

$$\lambda_{1/2} = \min \left\{ z' : \int_{-z'}^{z'} \langle \rho \rangle_z dz > \frac{1}{2} \Sigma_g \right\}. \quad (31)$$

At the start of the simulation this is related to the scale height by our choice of isothermal density profile, at  $\lambda_{1/2} = (1/2)b \log 3$ . Large outflows will ‘puff-up’ the disc to greater scale heights, at late times this would become inconsistent with our star formation profile.

(vi) Effective cooling rate,  $\eta_{\text{eff}}$ , is the total radiative cooling rate in the simulation volume divided by the mean SNe energy injection rate,

$$\eta_{\text{eff}} = \frac{\int_V \Lambda n^2 dV}{\int_{\text{area}} E_{\text{SN}} \in_{100} (\dot{\Sigma}_*/100 \text{ M}_{\odot}) dA}. \quad (32)$$

Conservation of energy implies that all of the energy not released as radiation must end up either in the wind or as gravitational potential energy. Due to the discrete nature of time sampling with snapshots (i.e. for many of the quantities such as cooling and we have instantaneous measurements of their time derivatives and not

measurements of the integrated quantities themselves), there is some error on our estimate of the integrated quantities. Most susceptible is the estimate of the cooling rate; the tail of high-density gas, seen in the density probability distribution function of Fig. 2, cools very rapidly, and our time sampling means its contribution to cooling is underestimated. We will inevitably miss some cooling that would have occurred outside the simulation volume (although much of this gas is tenuous and will have a long cooling time, little gas remains dense in the outflowing material). Nevertheless, our high snapshot frequency run gives us energy conservation to  $\sim 1$  per cent and confidence that we can accurately measure the outflowing components from the low-frequency runs (energy conservation in the simulation itself is of course much better than this).

In Fig. 5, we inspect these parameters for the simulation in Fig. 4. For the first  $\sim 2$  Myr, the most notable feature is the rapid increase of porosity as the SN blasts evacuate bubbles in the disc. The height of the disc remains approximately constant. As the simulation evolves, the remaining gas fraction declines (black curve) as gas leaves the simulation volume (blue curve). The mass lost from the simulation appears to be a nearly linear function of time at this stage, suggesting a constant outflow rate, which we investigate further in Section 5.

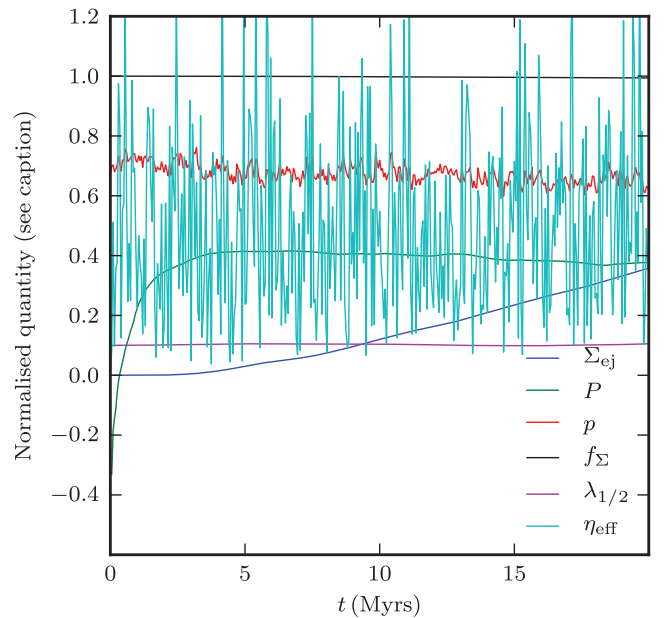


**Figure 5.** Generation of an outflow in the run in Fig. 4 as characterized by the evolution of normalized quantities described in (i)–(v) in the text. After a transient initial stage of  $\sim 5$  Myr, gas starts to be ejected at a nearly constant rate of  $\sim 0.01 \text{ M}_{\odot} \text{ Myr}^{-1} \text{ pc}^{-2}$ . The dark blue line is the cumulative mass ejected per unit area, in units of  $0.2 \text{ M}_{\odot} \text{ pc}^{-2}$ . The porosity  $P = -\log(f_{\text{cold}})$  of hot gas builds very quickly, the green line is  $0.5 + 0.2P$ , implying a filling factor of the HIM of approximately 50 per cent. The red line is the mean pressure,  $\log_{10}(p/10^3 \text{ K cm}^{-3})$ , disturbed from its initial value of  $0.7 \times 10^3 \text{ K cm}^{-3}$  in the base of the disc by the action of the SNe. The black line is the fraction of gas remaining in the simulation. The magenta line is the evolution of the scale height, equation (31), in terms of  $0.1\lambda_{1/2}(t)/\lambda_{1/2}(0)$ . The highly stochastic cyan line is  $\eta_{\text{eff}}$ , the instantaneous cooling rate as a fraction of the mean SNe energy injection rate. During the first  $\sim 2$  Myr the porosity in the simulation rapidly increases, after which the material begins to be ejected from the simulation in a relatively linear fashion. There are periods where the cooling rate increases dramatically by a factor of  $\sim 10$ , which are closely related to SN energy injection events. Energy injection has not significantly puffed up the disc.

<sup>4</sup> The pressure equilibrium predicted by Spitzer (1956) holds over smaller spatial scales where the supersonic turbulence decays over the sound crossing time.



### 4.3 Comparison to a rarefaction zone

A characteristic feature of both simulated and observed outflows (Steidel et al. 2010) is that the wind speed *increases* with height  $z$  above the disc, and it has been suggested that radiation driving is the cause of this (Murray, Quataert & Thompson 2005). Since radiation driving is not included in our modelling yet the outflow does accelerate, we suggest the following physical model. The combined effects of several SN explosions cause the ISM pressure to increase substantially above the hydrostatic equilibrium value. If gravity is not dominant, this will lead to the higher pressure ISM expanding into the lower pressure regions above the disc. In the launch region of such an outflow, 1D (plane-parallel) symmetry is a reasonable description of the geometry. A useful comparison is the behaviour of a rarefaction wave, where a homogeneous static gas is released into a sparse, pressure free zone, and for which the similarity solution is

$$\begin{aligned} v(\eta) &= \frac{2}{\gamma + 1} c_0 (1 + \eta), \\ \rho(\eta) &= \rho_0 \left( \frac{2}{\gamma + 1} - \frac{\gamma - 1}{\gamma + 1} \eta \right)^{2/(\gamma - 1)}, \\ \eta &\equiv \frac{z}{c_0 t}, \end{aligned} \quad (33)$$

valid for

$$\eta \in \left[ -1, \frac{2}{\gamma - 1} \right]. \quad (34)$$

In such a flow, speed increases with height  $z$  and density decreases. This is distinct from the flow due to a single blast wave, since in the Sedov-Taylor phase density *increases* with distance from the blast, which is not the case for the disc outflow (Fig. 1). Notably this does not describe a *steady* wind, which would be the result of continuous energy injection.

In a rarefaction wave, the acceleration is due to the pressure gradient in the outflow, and results in thermal energy being converted into kinetic energy, and the asymptotic flow speed is  $v_{\max} = 3c_0$  for  $\gamma = 5/3$ . The outflowing gas above the disc is mainly warm ISM gas that is entrained by the hot SN bubbles that power the rarefaction wave. Fig. 6 shows the behaviour of the simulation to be consistent with this model; velocity increases with height  $z$ , but decreases with time at a given height in a way predicted by the similarity solution.

Notably the rarefaction is not a steady-state solution, and thus is not a good description of the time-averaged behaviour of the gas. Such behaviour should mimic the result of continuous energy injection, where multiple overlapping SNe in the form of rarefactions or ST blast waves (see e.g. Castor, McCray & Weaver 1975; Weaver et al. 1977; McCray & Kafatos 1987) drive a large-scale wind. Our simulations are sufficiently stochastic however that we shall leave this for future work. There will also be departures from a steady-state solution as the disc consumes its gas, or in a real galaxy, has some gas inflow.

### 4.4 Absorption features of galactic winds

Steidel et al. (2010) propose that the C II absorption line data are also well fitted with velocities increasing with distance from the disc (in particular, the lower panel of fig. 24 of Steidel et al. 2010). The explanation above provides a physical mechanism for those measured features. This is without the radiation and dust-driven mechanisms invoked by Murray et al. (2005), Martin (2005) and Sharma, Nath & Shchekinov (2011).

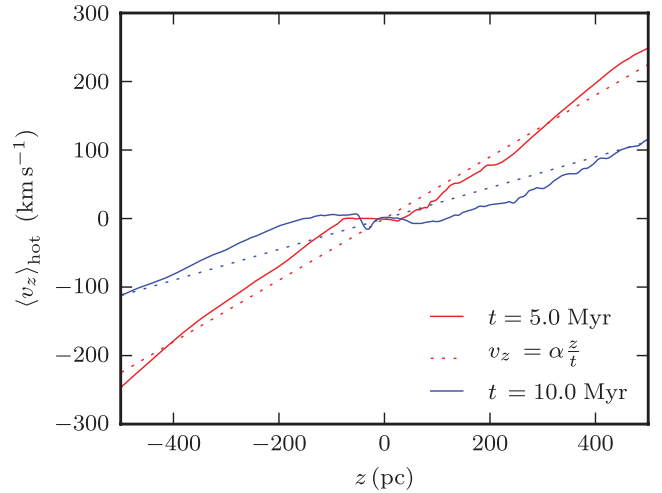


**Figure 6.** The solid line shows the mean vertical velocity as a function of height for two times in the  $\Sigma_g = 2.5 M_\odot \text{ pc}^{-2}$ ,  $f_g = 0.01$  simulation showing only the hot gas (where we have defined hot gas to be that above  $2 \times 10^4$  K). The red dotted line is a linear fit ( $\alpha = 2.6$ ) to the earlier snapshot ( $t = 2.5$  Myr) which is then extrapolated to the later snapshot (blue dotted line). This shows that the profile is evolving in an approximately self-similar fashion with the hot material accelerating away from the disc primarily due to its thermal energy being converted into kinetic energy.

We pointed out in Fig. 1 the multi-phase nature of the outflow, as well as the fact that outflow speed depends on temperature. This is made more vivid in Fig. 7 in which we show mock ‘absorption lines’ of gas selected in narrow temperature bins. These mock line profiles are simply the fraction of gas in a given temperature range, that is moving with a given velocity, as a function of velocity,  $v$ . For the temperatures  $T < 10^7$  K, the lines have their highest optical depths at  $v \sim 0 \text{ km s}^{-1}$ , and shapes which vary little with temperature  $T$ , and are almost symmetric in velocity. The line shapes broaden as the temperature increases, and for the hottest gas at  $T > 10^7$  K the line becomes asymmetric and the absorption centre is now  $\sim -100 \text{ km s}^{-1}$ . It is tempting to compare these to absorption line studies in outflows such as Martin (2005) in Na I and Weiner et al. (2009) in Mg II; however, more work would be required to calculate corrections for the geometry and ionization.

Fig. 1 also shows colder clouds entrained inside the much hotter flow, with cometary-like tails where the cloudy medium is being ablated by the hot gas rushing past. Absorption lines might arise from mass loading this hot flow either through conductive evaporation (see e.g. Boehringer & Hartquist 1987; Gnat, Sternberg & McKee 2010) and/or through ablation (e.g. Hartquist et al. 1986). Fujita et al. (2009) investigated the warm clouds in axisymmetric 2D simulations, where the clouds appear as Rayleigh–Taylor unstable cool shells and fragments that can explain the high-velocity Na I absorption lines. We note that the metallicity of the gas phases is likely to be quite distinct, as the SNe are both the origin of the heating and of the metals, and we intend to explore this in a subsequent paper.

## 5 THE DEPENDENCE OF OUTFLOWS ON DISC PROPERTIES

In the previous section, we have discussed in detail the features of a simulation of an SN-driven wind using a set of fiducial parameters for the disc and SN rate, the processes which drive it and the statistics that can be used to examine it. In this section, we explore how the

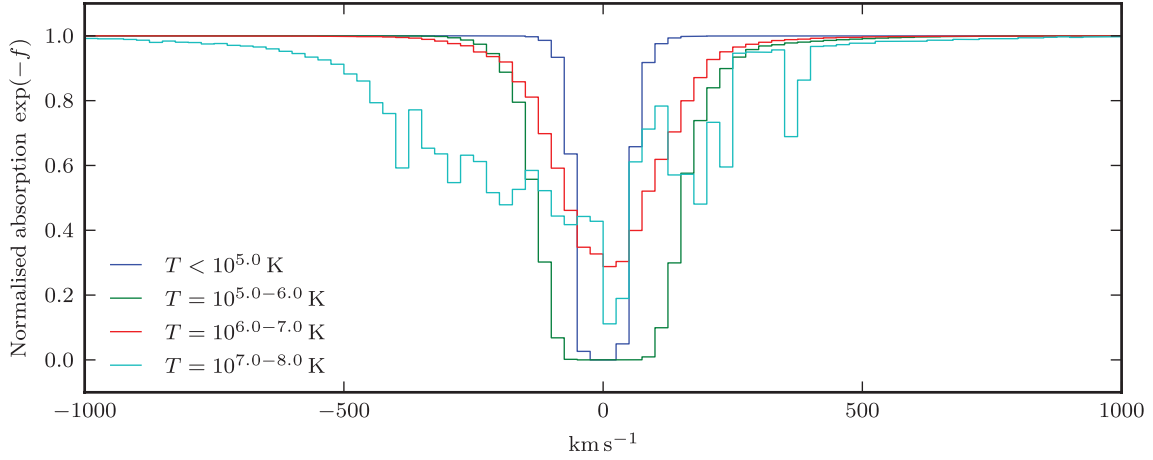


**Figure 7.** Normalized column density as a function of velocity, for gas with different temperatures (coloured lines). For low-temperature absorbers ( $\lesssim 10^6$  K), we see a single-peaked profile centred around the rest-frame velocity of the disc. For higher temperature absorbers, we see absorption at higher velocities relative to the disc, with velocity increasing with temperature. Only the  $\gtrsim 10^7$  K distribution appears to show any significant asymmetry.

outflow properties vary and scale with the parameters. We will use such scalings in the next section to integrate over a full galactic disc.

In Fig. 8 we plot average velocities above the simulation disc, for the simulations varying  $\Sigma_g$  and  $f_g$ . There appears to be a strong trend in wind velocity, with wind speed increasing with increasing gas surface density, but decreasing gas fraction. There are no simulations in the upper left as these would have a scale height larger than half the box size, or in the lower right as these would have a scale height less than 3 pc.

### 5.1 Mass outflow

Inspecting the ratio of mass outflow rate to star formation rate gives us an analogous property to that of equation (1), i.e. for a specific area on the disc

$$\beta = \frac{\dot{\Sigma}_{ej}}{\dot{\Sigma}_*}, \quad (35)$$

which we use in our subsequent analysis. In theory every snapshot from our simulations contains an estimate of this  $\beta$ , as the mass outflow rate at a specific height; however, this is rather stochastic, and as an alternative we calculate  $\beta$  as a fit to several measurements of the integrated outflow

$$y_i = \frac{\int_0^{t_i} \dot{\Sigma}_{ej} dt}{\int_0^{t_i} \dot{\Sigma}_* dt}, \quad (36)$$

which are easily obtained from each simulation snapshot. We fit the data samples  $\{(t_i, y_i)\}_{i=1}^n$  with the ramp function

$$f(t) = \begin{cases} 0, & t < t_0 \\ \beta t, & t \geq t_0, \end{cases} \quad (37)$$

where the parameters  $t_0$  and  $\beta$  are free variables. The motivation for choosing such a fit is that, whilst the ejection rate is nearly linear in most cases, there is a time ( $t_0$ ) required for the system to reach a quasi-steady state. This will not be a true steady state, in that the wind will eventually exhaust the supply of cold gas; however, this occurs over a sufficiently long time-scale that the fit is a reasonable description for our simulations.

The square error of this function can be analytically solved by finding linear regressions for the subsets  $s_k$  of  $\{(t_i, y_i)\}_{i=1}^n$  defined by  $\{(t_i, y_i)\}_{i=k}^n$  and choosing the minimum  $k$  such that the linear

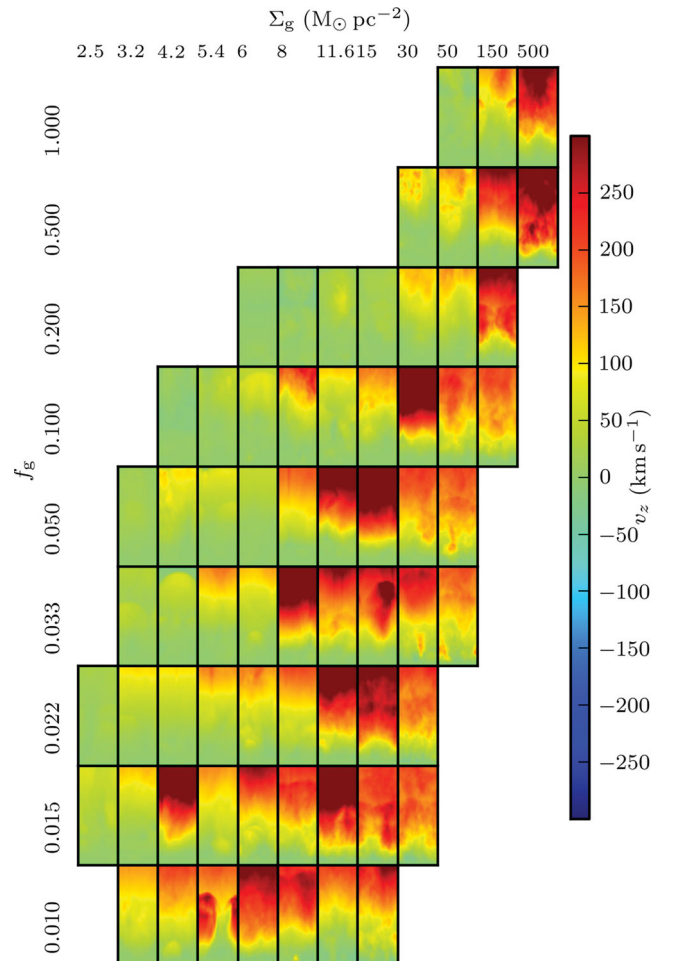


**Figure 8.** Matrix view of simulations varying gas surface density ( $\Sigma_g$ ) and gas fraction ( $f_g$ ), each panel showing a time-averaged vertical velocity for the upper half plane of each simulation (i.e. the disc is at the base of each panel). Gas surface density increases from left to right, gas fraction increases from bottom to top. There appears to be a strong trend in wind velocity towards the lower right-hand panels, i.e. a disc with low gas fraction but high gas surface density tends to generate a faster wind.

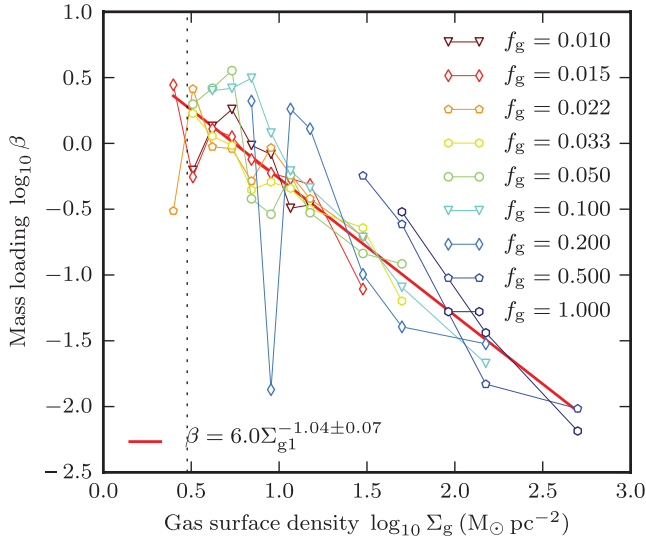


**Figure 9.** The mass loading  $\beta$  (mass ejection rate versus rate of star formation) as a function of gas surface density  $\Sigma_g$ . Each point represents a fit of  $\beta$  (Section 5) to star formation simulations of varying  $\Sigma_g$  and  $f_g$ . The red line denotes a power-law fit with jackknife errors, coloured symbols (red–blue) correspond to the simulations with gas fraction  $f_g = 0.01$ – $1.0$ , respectively. The vertical grey dashed line indicates the  $3 \text{ M}_\odot \text{ pc}^{-2}$  threshold for star formation from Schaye (2004). We see a significant negative dependency of  $\beta \sim (\Sigma_g / 1 \text{ M}_\odot \text{ pc}^{-2})^{-1.04 \pm 0.07}$  on the gas surface density, which may be due to the larger gravitational potential or the higher rate of cooling (incurred by higher gas densities) or some combination of both. We also note that the scatter seems partially a function of  $f_g$ , with higher gas fractions showing larger values of  $\beta$  than the lower (e.g. blue versus green).

regression  $t$ -intercept  $< t_k$ . If we define  $g(s_k)$  as the  $t$ -intercept of the linear regression for  $s_k$ , then

$$t_0 = \min \{ t_k : g(s_k) < t_k, s_k \equiv \{(t_i, y_i)\}_{i=k}^n \}, \quad (38)$$

and  $\beta$  is the slope of this linear regression.

Plots of the gas fraction remaining in the simulation volumes can be seen in Fig. 5 for the fiducial model, and for the set of simulations of varying  $\Sigma_g$  and  $f_g$  in Fig. A9 where we also show the fits given by equation (37).

In Fig. 9, we plot the mass loading  $\beta$  as a function of gas surface density  $\Sigma_g$ . Each point represents a fit of  $\beta(\Sigma_g)$  for the simulations varying  $\Sigma_g$  and  $f_g$ . The first point to note is that our  $\beta$  values all lie below 4, and for a large range of our parameters  $\beta \ll 1$ , i.e. our domain of parameter space switches from effective feedback (more gas ejected than stars formed) to ineffective, where the amount of gas released is much smaller than that converted into stars.

Based on jackknife errors, our power-law fit shows a significant negative dependency,  $\beta \approx 6 (\Sigma_g / 1 \text{ M}_\odot \text{ pc}^{-2})^{-1.04 \pm 0.07}$ , implying that at high gas surface densities the feedback is less efficient. This could be due to a number of effects. Since a higher gas surface density will correspond to a deeper potential well, the escape velocity of the gas is higher. Secondly, the higher gaseous surface densities correspond to higher gas volume densities (equation 19), resulting in shorter cooling times.

Another notable dependency is that on the gas fraction. Some of the scatter seen in Fig. 9 actually depends systematically on the gas fraction,  $f_g$ , with higher gas fractions showing consistently larger  $\beta$  values than the lower values. We explore this in Fig. 10, where

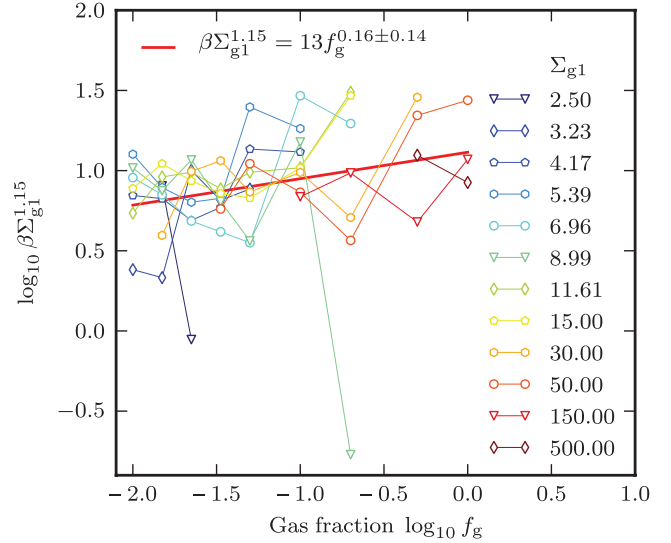


**Figure 10.** Joint dependence of the mass loading  $\beta$  on gas surface density,  $\Sigma_g$ , and gas fraction  $f_g$ . Differently coloured curves correspond to simulations with different values of  $\Sigma_{g1} \equiv \Sigma_g / \text{M}_\odot \text{ pc}^{-2}$ , the thick red line is our best fit of the simulation points. We see a dependence of  $\beta \Sigma_g^{1.15}$  on gas fraction, with a power-law dependency of  $0.16 \pm 0.15$ . Higher gas fractions for a given gas surface density imply a shallower potential well, explaining why the outflow efficiency increases with  $f_g$ .

we have performed a simultaneous fit of  $\beta$  to both the gas surface density and the gas fraction,

$$\beta = \beta_0 \Sigma_g^{-\mu} f_g^\nu, \quad (39)$$

where we find the values

$$\beta_0 = 13 \pm 10, \quad (40)$$

$$\mu = 1.15 \pm 0.12, \quad (41)$$

$$\nu = 0.16 \pm 0.14. \quad (42)$$

By construction, the joint fit now no longer shows a systematic dependence on either  $\Sigma_g$  or  $f_g$ .

Accounting for this shows a positive dependency of  $f_g^{0.16 \pm 0.14}$ , i.e. by holding the gas surface density constant but increasing the gas fraction (which reduces the gravitational strength, thus increasing the dynamical time and reducing the star formation rate) increases the mass loading. As with the dependence on gas surface density, we are effectively seeing a sublinear dependence on star formation rate, as we decrease the star formation (increase the gas fraction), we see a less than proportionate drop in the outflow rate. Again, the mechanism causing this should be a combination of the processes for the  $\Sigma_g$  dependence, derived above.

In Fig. 10 there is considerable scatter, especially at high gas fraction where a number of simulations have mass ejection rates considerably above the trend. This is most likely due to heavy disruption of the disc out of the plane where the wind from subsequent SNe can eject it from the simulation volume. With such stochasticity, the description of all the simulations with a simple power law becomes inadequate.

Our measured value for the exponents  $\mu = 1.15$  and  $\nu = 0.16$  that relate mass loading to gas surface density and gas fraction,  $\beta \propto \Sigma_g^{-\mu} f_g^\nu$ , can be compared with the values from the model described

in Section 4.1.1, which predicts scalings of  $\mu = 8/11 = 0.72$  and  $\nu = 4/11 = 0.37$ . That model does not include gravity, and we suggest this is why the measured and predicted values differ. To verify this we have performed a series of simulations with significantly higher star formation rate, described in Appendix A. This uses a slightly different parametrization that is more commonly used in cosmological simulations which introduces an extra dependence on the gas fraction, but the primary effect is an increase in star formation for the parameter range we study. In these runs, the energy injection rate is much higher, the volume filling factor of the hot phase much larger, and the outflow rates are correspondingly larger as well. Consequently, the effect of gravity of the disc is much reduced. Fitting  $\beta \propto \Sigma_g^{-\mu} f_g^\nu$  to these runs yields  $\mu = 0.82$  and  $\nu = 0.48$ , in much better agreement with the predictions of the simple model.

It would be interesting to extend the model to account for the gravity of the disc, along the lines followed by Stringer et al. (2011). Assume that the  $\beta$  of the hot gas in equation (29) is modified by an escape fraction  $f_{\text{esc}}$ , which is equal to the fraction of material that has a temperature above the escape temperature of the simulation volume. Assuming the outflow has a range of temperatures, characterized by a Maxwell–Boltzmann distribution, and that only gas with  $T > T_{\text{esc}}$  escapes, the fraction is

$$f_{\text{esc}} = \int_{T_{\text{esc}}} f(T) dT \approx 1 - \frac{4}{3\sqrt{\pi}} \left( \frac{T_{\text{esc}}}{T_s} \right)^{3/2}. \quad (43)$$

We have assumed that  $T_{\text{esc}} \ll T_s$ , i.e. the low energy tail of the distribution fails to escape. The net outflow will thus drop faster at high  $\Sigma_g \propto T_{\text{esc}}$ , making the dependence of the mass loading on  $\Sigma_g$  stronger, which is consistent with the higher  $\mu \approx 1.15$  we see in the lower star formation rate simulations.

## 5.2 Radiative efficiency and energy partition in the ISM

Whilst the mass loading of the galactic wind is one of the most cosmologically significant parameters to study, we would also like to evaluate the energy budgets and structure of the winds in our simulations. The energy injected by the SNe is absorbed into the gravitational binding energy, distributed into thermal and mechanical energies (both in the bulk motion of the wind and in turbulence throughout the simulation volume) and released as radiation (via cooling).

The energy partition also enables us to evaluate a wind velocity for the galaxy, which is commonly used to characterize feedback models for galaxy formation (e.g. Bower et al. 2012). The fraction of the energy that is incorporated into the wind, in combination with the mass loading, determines the overall wind speed for a galaxy. This is an important parameter in determining whether the wind can leave the galaxy and hence provide efficient quenching of star formation.

By examining our simulations, we can determine the fractions of energy that have been converted into the different modes. In our fiducial simulation, we discover that a fraction of 87 per cent was radiated, 4.5 per cent was advected out of the computational volume as thermal energy, 5 per cent as mechanical energy (with over half of this in the form of turbulent energy), 1 per cent went

into heating the simulation volume,<sup>5</sup> 1 per cent went into turbulence in the simulation volume and a rather low 0.5 per cent went into puffing-up the disc. The parameters here are averaged in a similar manner to the mass ejection rate, by taking the mean over snapshots after  $t_0$  (equation 38), i.e. in the quasi-steady regime.

Summation of these quantities allows us to estimate  $\eta_T$  (equation 5), the fraction of power that is thermalized into the outflow,

$$\eta_T = \eta_{\text{therm}} + \eta_{\text{mech}}, \quad (44)$$

i.e. the sum of the thermal and mechanical (bulk and turbulent) contributions (the remainder going almost entirely into cooling). This allows us to calculate an effective velocity  $v_{\text{eff}}$  for the wind,

$$v_{\text{eff}} = \sqrt{\frac{2\eta_T}{\beta} \left( \frac{E_{\text{SN}} \varepsilon_{100}}{100 M_\odot} \right)}, \quad (45)$$

where we have combined the equation for mass loading,  $\beta \equiv \dot{M}_{\text{wind}}/\dot{M}_*$ , and the thermalization of SN energy into the kinetic energy of the wind ( $\eta_T$ ), to find the specific energy in the wind (i.e. an inversion of equation 5). Notably this will be significantly higher than the wind velocities we see at the edge of our simulation volume because it includes the energy of the thermal and turbulent components. At larger distances from the galaxy, however, we expect this to be a more realistic estimate, as the thermal energy accelerates the wind and is converted into the mechanical energy of the bulk flow. This is a consequence of our simulations focusing on the launch region of the galactic wind, and hence the wind has not yet reached its terminal velocity. Note that ram pressure from infalling gas may be an important obstacle in slowing down or even preventing the outflowing gas from escaping (e.g. Theuns et al. 2002).

In Fig. 11 we explore the dependence of the mass loading  $\beta$ , the fraction of power in the outflow,  $\eta_T$ , and the effective wind velocity,  $v_{\text{eff}}$ , as a function of the total surface density of the disc,  $\Sigma = \Sigma_g/f_g$ . In terms of the mass loading, we see a negative dependence on surface density; for comparison, we have also included the power-law fit from equations (40)–(42).

The fraction of power released to the wind,  $\eta_T$ , appears to be correlated almost entirely with gas fraction  $f_g$ , at high gas fractions much of the energy of star formation is simply radiated away, which is intuitive since the higher gas fractions will have shorter cooling times. For comparison we also show values of  $\eta_T = 0.1$  and 0.4 (the former being the equivalent to the widely quoted 10 per cent efficiency in Larson 1974); we find star formation in discs to lie close to this value, except at very low gas fractions.

The fall in outflow power in Fig. 11 at low surface densities can also be seen as a fall in the effective wind velocity. Here we have converted our sample values of  $\eta_T = 0.1$  and 0.4 into effective wind velocities using the power-law fit for  $\beta$  in equations (40)–(42). Each gas fraction appears to follow a line of approximately constant  $\eta_T$ , although there is some suggestion of a change in slope below  $\Sigma = 10^2 M_\odot \text{pc}^{-2}$ .

## 6 IMPACT OF OUTFLOWS ON GALAXY EVOLUTION

In this section, we apply our results from the previous section to the mass outflow from disc galaxies of different masses. We will assume a surface density profile for a galaxy and use our fits for

<sup>5</sup> Note that in a true steady state this fraction should be compensated by cooling.



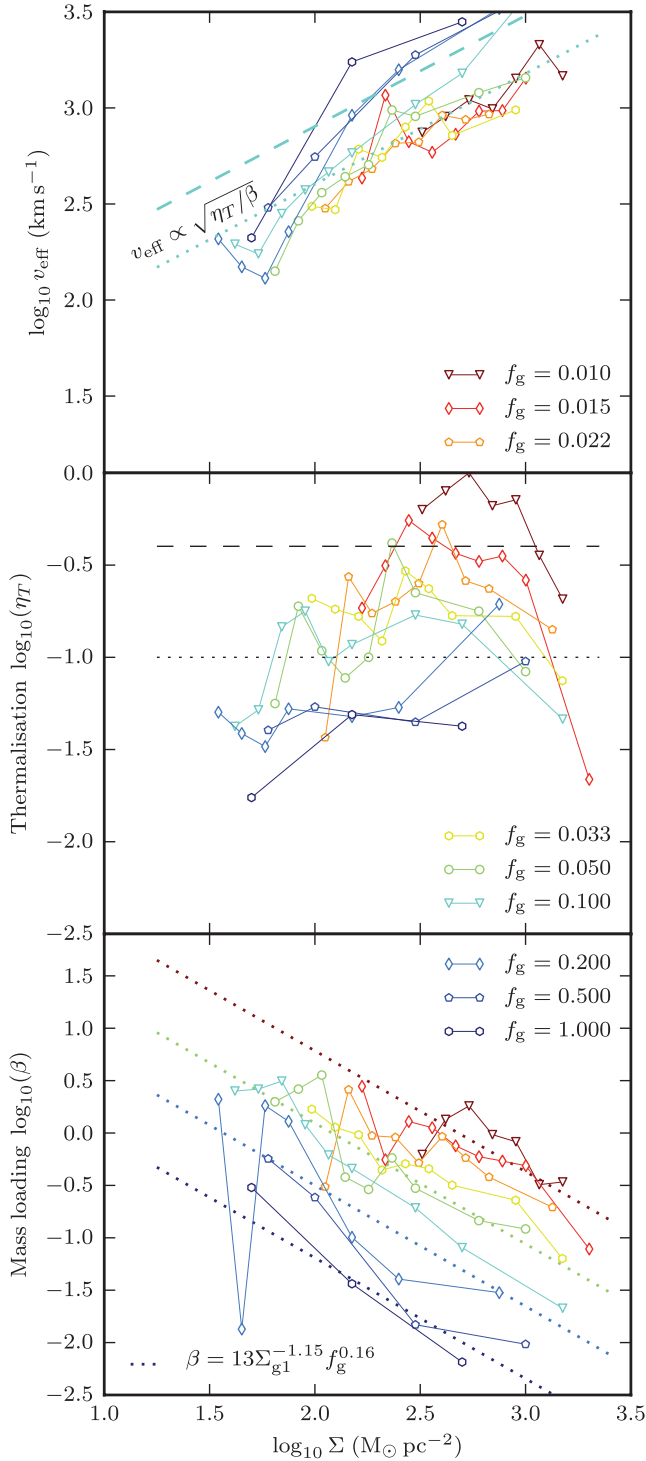


**Figure 11.** Effective wind speed (upper panel), outflow efficiency (middle panel) and mass loading (lower panel) as a function of total surface density  $\Sigma = \Sigma_g/f_g$ . Coloured lines with symbols are the simulations from Figs 9 and 10, with values of the gas fraction  $f_g$  as indicated. Dotted lines in the lower panel are the scalings from equations (40)–(42), plotted for  $f_g = 0.01, 0.015, 0.2$  and  $1.0$  in the corresponding colours. Lines of constant efficiency,  $\eta_T = 0.1$  and  $0.4$ , are shown in the middle panel (black dotted and dashed, respectively). Curves for the corresponding scaling of the effective wind speed for  $f_g = 0.1$  are shown in the upper panel. The outflow efficiency increases with surface density, as does the effective wind speed.

outflow efficiency as a function of surface density, to deduce an overall feedback efficiency.

### 6.1 Dependence on circular velocity from theoretical arguments

In this section, we take our measured dependencies of the mass loading parameter (which are derived for a patch of the ISM) and apply them to an entire disc galaxy by integrating over the surface of the disc. This will allow us to compare with feedback schemes considered in Cole et al. (2000), Bower et al. (2006), etc., which introduce a relation between circular velocity, mass loading and effective wind speed.

Our first step is to assume a model for a disc galaxy inside a dark matter halo where we follow Mo, Mao & White (1998). The circular velocity of a spherical isothermal dark halo of mass  $M_{200}$  is given by

$$V_{200}^3 = 10 G M_{200} H(z) \quad (46)$$

(Mo et al. 1998), where  $H(z)$  is the Hubble parameter as a function of redshift,  $z$ . Since the baryonic component can release energy via cooling, it can collapse further to become a rotationally supported disc. Observed bulgeless discs have a near-exponential profile in luminous mass of the form

$$\Sigma(r) = \Sigma_0 \exp(-r/R_d), \quad (47)$$

with normalization  $\Sigma_0$  and scale length  $R_d$ . The mass of the disc is thus given by

$$M_d = \int_0^\infty 2\pi \Sigma(r) r dr = 2\pi \Sigma_0 R_d^2. \quad (48)$$

The scale length  $R_d$  is controlled by the specific angular momentum of the material forming the disc (e.g. Fall & Efstathiou 1980). An exponential disc with constant rotation velocity  $V_d$  has angular momentum

$$J_d = 4\pi \Sigma_0 V_d R_d^3, \quad (49)$$

and if we parametrize in terms of the disc mass as a fraction of the halo mass,  $m_d \equiv M_d/M_{200}$ , the circular velocity of the disc as a fraction of the halo's,  $v_d = V_d/V_{200}$  and the specific angular momentum fraction of the disc  $j_d/m_d$ , we can infer the surface density normalization to be

$$\begin{aligned} \Sigma_0 &= \frac{2}{\pi} \frac{M_d^3 V_d^2}{J_d^2} \\ &= \frac{10 H(z)}{\pi G} \lambda^{-2} \left( \frac{j_d}{m_d} \right)^{-2} m_d v_d^2 V_{200}, \end{aligned} \quad (50)$$

where  $\lambda$  is the spin parameter of the isothermal halo in equation (46). Notably if we set  $v_d = 1$  we recover the Mo et al. (1998) surface density equation, yet for real discs  $v_d > 1$  as the contribution of baryons to the rotation velocities is not insignificant.

We can now compute a mean mass loading  $\hat{\beta}$  for such a galaxy, by evaluating

$$\hat{\beta} \equiv \frac{\dot{M}_{\text{wind}}}{\dot{M}_*} = \frac{\int 2\pi \beta \dot{\Sigma}_* r dr}{\int 2\pi \dot{\Sigma}_* r dr}, \quad (51)$$

where we will assume that the surface density in star formation,  $\dot{\Sigma}_*$ , follows the KS relation:

$$\dot{\Sigma}_* = A \Sigma_g^n. \quad (52)$$

Taking the dependence of mass loading on surface density found from our fits to the simulations, equation (39), then equation (51)

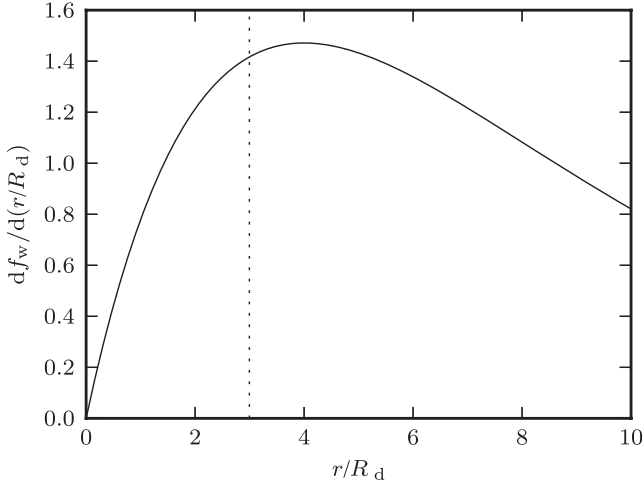


**Figure 12.** Fraction of the wind launched at each radius in the disc (equation 54), for a KS relation  $\dot{\Sigma}_* \propto \Sigma_g^n$ , with  $n = 1.4$ , and assuming mass loading scales with gas surface density as  $\beta \propto \Sigma_g^{-\mu}$ , with  $\mu = 1.15$  (equation 41). The dotted line indicates the characteristic wind radius  $R_w/R_d$  for the galaxy, where the local mass loading equals the net mass loading for the galaxy as a whole,  $\hat{\beta} = \dot{M}_{\text{wind}}/\dot{M}_*$ .

can be integrated analytically. We rewrite equation (39) in terms of the total surface density,  $\Sigma$ , and the gas fraction,  $f_g$ , and obtain

$$\beta(\Sigma, f_g) = \beta_0 \left( \frac{\Sigma}{1 \text{ M}_\odot \text{ pc}^{-2}} \right)^{-\mu} f_g^{v-\mu}, \quad (53)$$

giving a dependence on the gas fraction,  $\propto f_g^{-0.99}$ . The fraction of the wind launched as a function of radius is given by

$$\begin{aligned} \frac{df_w}{d(r/R_d)} &= \frac{2\pi R_d \beta(r) \dot{\Sigma}_*(r)}{\dot{M}_{\text{wind}}} \\ &= (n - \mu)^2 \left( \frac{r}{R_d} \right) \exp[-(n - \mu)r/R_d], \end{aligned} \quad (54)$$

which gives the differential rate of production of the star formation driven wind, normalized by the total wind. This function is plotted in Fig. 12. At large radii the star formation is most effective at driving a wind, but the net contribution to the galaxy outflow is limited by the low rate of star formation there. Conversely at small radii the wind is limited by the small area of the disc, and so it is at intermediate radii where the local mass loading equals that of the galaxy as a whole.

We can characterize this further by defining a wind radius  $R_w$  by

$$\hat{\beta} = \beta(\Sigma(R_w), f_g), \quad (55)$$

that is,  $R_w$  is that radius in the galaxy where the local mass loading,  $\beta = \dot{\Sigma}_{\text{ej}}/\dot{\Sigma}_*$ , equals the total mass loading of the entire galaxy,  $\hat{\beta} = \dot{M}_{\text{wind}}/\dot{M}_*$ . The wind radius for the galaxy is then given by

$$\begin{aligned} R_w &= \frac{2}{\mu} \ln \left( \frac{n}{n - \mu} \right) R_d \\ &\approx 3.0 R_d, \end{aligned} \quad (56)$$

where we have substituted in  $n = 1.4$  for the exponent in the KS relation, and used the values for  $\mu$  from equation (41). For the MW, a disc scale length of  $R_d = 2.5$  kpc gives a wind radius of  $R_w = 7.5$  kpc, inside the solar radius but outside the galactic bulge. We have neglected the fact that there will not be any star formation far out in the disc if the gas surface density drops too low, as well as

the presence of a bulge, where there may be little gas and hence also little star formation. This will lead us to overestimate the wind in the tails of Fig. 12.

To parametrize feedback in terms of the circular velocity,  $V_{200}$ , we apply equation (50) and use our fiducial values of  $\beta_0$ ,  $\mu$ ,  $v$  and  $f_g$  to find

$$\begin{aligned} \hat{\beta} &= \beta_0 \left( \frac{n}{n - \mu} \right)^2 \left( \frac{\Sigma_0}{1 \text{ M}_\odot \text{ pc}^{-2}} \right)^{-\mu} f_g^{v-\mu} \\ &\approx 10 \left( \frac{\beta_0}{13} \right) \left( \frac{f_g}{0.2} \right)^{v-\mu} \left( \frac{j_d}{m_d v_d} \right)^{2\mu} \\ &\quad \times \left[ \left( \frac{\lambda}{0.05} \right)^{-2} \left( \frac{V_{200}}{155 \text{ km s}^{-1}} \right) \left( \frac{m_d}{0.03} \right) \frac{H(z)}{H_0} \right]^{-\mu}, \end{aligned} \quad (57)$$

where we also assumed  $H_0 = 71 \text{ km s}^{-1} \text{ Mpc}^{-1}$  (Freedman et al. 2001).

To convert to disc properties, we can eliminate the spin parameter with

$$R_d = \frac{\lambda V_{200}}{\sqrt{200} H(z)} \left( \frac{j_d}{m_d v_d} \right). \quad (58)$$

Setting  $j_d/m_d$  and  $v_d$  as unity, however, yields an MW with a rather low circular velocity ( $155 \text{ km s}^{-1}$ ) and scale length considerably higher.

The formation of the baryonic disc can increase the rotation velocities from  $V_{200}$  both directly and indirectly. The baryons make their own contribution to the gravitational potential, and can also induce changes in the profile of the dark matter, for example due to adiabatic contraction (e.g. Mo, van den Bosch & White 2010). Even without baryons, there will be some adjustment to  $v_d$  due to the non-isothermal nature of haloes (Navarro, Frenk & White 1997), i.e. a dependence on the concentration parameter. Here we will take  $v_d = 1.29$  to give a circular speed of  $V_d = v_d V_{200} = 200 \text{ km s}^{-1}$ , similar to the value of the MW (Dehnen & Binney 1998; Flynn et al. 2006, but see also Reid et al. 2009 that has the speed closer to  $250 \text{ km s}^{-1}$ ).

Having set the circular speed, the disc scale length is implied by the specific angular momentum fraction in equation (58). For the 2.5-kpc disc of Flynn et al. (2006) we set  $j_d/m_d = 0.42$ , i.e. the disc is preferentially formed of the low angular momentum baryons. A possible reason for the lower specific angular momentum is the delayed collapse of baryons in the disc due to photoheating (since discs grow in an inside-out manner, with the low angular momentum material accreted first; Navarro & Steinmetz 1997).

Finally, we should mention that the spin parameter of the MW may differ from 0.05, and indeed recent simulations that remove transient objects from haloes have suggested that haloes have a smaller  $\lambda$  (e.g. Bett et al. 2007); however, we have made no account for this as it is outside the scope of this model.

With these new parameters, the MW disc has a more realistic higher surface density, and equation (57) becomes

$$\begin{aligned} \hat{\beta} &\approx 0.31 \left( \frac{\beta_0}{13} \right) \left( \frac{f_g}{0.2} \right)^{v-\mu} \\ &\quad \times \left[ \left( \frac{V_d}{200 \text{ km s}^{-1}} \right)^3 \left( \frac{R_d}{2.5 \text{ kpc}} \right)^{-2} \left( \frac{m_d}{0.03} \right) \frac{H_0}{H(z)} \right]^{-\mu}. \end{aligned} \quad (59)$$

The normalization and scaling with  $V_d$  we find are somewhat below our expectations for SN feedback. For an MW-like halo, the

star formation would remove less than one solar mass of gas for every solar mass of stars formed ( $\hat{\beta} \sim 0.31$ ). Nevertheless, haloes with smaller circular velocities with the same disc radius and disc mass fraction show increasingly effective feedback,  $\hat{\beta} \propto V_d^{-3.4}$ , a similar scaling to energy conserving winds (e.g. Stringer et al. 2011). Note that the power-law dependence on  $V_d$  is somewhat stronger than the value of  $-1$  found by Hopkins et al. (2011). Those authors also found an exponent of  $-0.5$  for the dependence of mass loading on surface density, which is weaker than our exponent in equation (59) of  $\hat{\beta} \propto \Sigma^{-1.15}$ . Whilst the agreement between these simulations is not particularly good, this is perhaps not surprising given that they are performed with some different physics, at different resolutions and using different hydrodynamical schemes.

Despite the appeal of the above framework in supplying us with predictions for the mass loading in terms of redshift and the disc properties, there is a caveat here in our adjustment of  $j_d/m_d$  and  $v_d$  to match the observed MW. Although we can derive this from observations for the MW, and the mechanism for this appears to be understood, it would be erroneous to suggest we have a consistent model for this, and current numerical simulations such as those of Scannapieco et al. (2011) have yet to converge on the properties of a disc for a single halo. Most concerning is that these quantities almost certainly have some implicit dependence on halo mass and thus there should be a corresponding adjustment to the scaling relation in equation (59).

## 6.2 Dependence from observed data

Given the approximate ingredients required to construct the formalism of the previous section, it is interesting to ask whether we can parametrize our fit to the mass loading, equation (57), with purely observational estimates, i.e. to compute the disc surface density from observed disc properties, side-stepping the models of Mo et al. (1998).

One particularly attractive method is to invert equation (48) to write the surface density in terms of the disc radius  $R_d$  and mass  $M_d$ , where the latter can be estimated from the circular velocity of the disc with the Tully–Fisher relation (Tully & Fisher 1977). A recent calibration of the baryonic Tully–Fisher relations gives  $M_d = 8 \times 10^{10} M_\odot (V_{\text{max}}/200 \text{ km s}^{-1})^4$  (Trachternach et al. 2009), application of which gives

$$\hat{\beta}_{\text{TF}} = 0.31 \left( \frac{\beta_0}{13} \right) \left( \frac{f_g}{0.2} \right)^{\nu-\mu} \times \left[ \left( \frac{V_d}{200 \text{ km s}^{-1}} \right)^4 \left( \frac{R_d}{2.5 \text{ kpc}} \right)^{-2} \right]^{-\mu}, \quad (60)$$

which is very close to the relation in equation (59), including normalization and the  $R_d$  scaling. The difference is in the exponent of  $V_d$ , and the dependence of equation (59) on  $m_d$ , which implicitly depends upon  $V_d$  as well.

In principle, it is possible to calculate the mass fraction in the disc from the stellar mass to halo mass function using an abundance matching approach, which would relate  $m_d$  to  $V_{200}$ . A single power law  $m_d \propto M \propto V_{200}^3$  is a good fit, although from equation (4) we see that there is a dependence on the faint end slope of the stellar mass function (and at higher masses a broken power law may be more appropriate, e.g. Yang, Mo & van den Bosch 2003; Guo et al. 2010; Moster et al. 2010). Substituting this relation for  $m_d$  in equation (60) then yields  $\hat{\beta} \propto V_{200}^{-6.9} R_d^{2.3}$  versus  $\hat{\beta}_{\text{TF}} \propto V_d^{-4.6} R_d^{2.3}$  from equation (60) (taking  $\mu = 1.15$  for both). Finally, we can

try to eliminate the dependence on  $R_d$ , assuming  $R_d \propto M_d^{0.15}$ , as inferred by Shen et al. (2003). This yields a scaling of  $\hat{\beta} \propto V_d^{-4.8}$  versus  $\hat{\beta}_{\text{TF}} \propto V_d^{-2.5}$ . The difference between these scalings is due to the discrepancies between the modelled and observed slope for the Tully–Fisher relation and the uncertainty in modelling the disc mass fraction.

Although both our scalings are strongly dependent on  $V_d$ , our  $\beta$  values were all in the range  $0.01$ – $4$ , so the change in feedback acts more like a switch. At low disc circular velocities ( $V_d \lesssim 140 \text{ km s}^{-1}$ ) the feedback is high ( $1 < \beta < 4$ ), and at higher disc velocities the feedback shuts off, all over a relatively small range in  $V_d$ .

To summarize, we have developed two approaches to analyse the mass loading for a galaxy based upon our estimates for the mass loading in our ISM patches. In Section 6.1, we take an analytic approximation to the properties of disc in their host haloes which allows us to trace the feedback with redshift. This does, however, require us to make assumptions about the scaling of the gravitational contribution of the baryonic discs and the preferential accretion of low angular momentum baryons, neither of which are fully understood. Section 6.2 has bypassed these model concerns by parametrizing the galaxies using the observed disc mass–velocity relation to directly apply the mass loadings. One price for this is the loss of the dependence on redshift and the cosmological evolution.

Although these two approaches lead to different scalings, they do give a consistent normalization for the feedback in the MW at redshift zero. In principle, one way to test this formalism is to apply it in phenomenological models such as GALFORM, where parameters such as  $j_d$ ,  $v_d$  and  $m_d$  are followed. We discuss this comparison further in the next section.

## 6.3 Comparison to cosmological models

We are now in a position to compare the outflow rate we measured in our high-resolution simulations with values assumed in semi-analytic models such as GALFORM (Cole et al. 2000). The feedback prescription for the original GALFORM was

$$\beta = \left( \frac{V_d}{V_{\text{hot}}} \right)^{-\alpha_{\text{hot}}}, \quad (61)$$

with values in the reference model of  $V_{\text{hot}} = 200 \text{ km s}^{-1}$  and  $\alpha_{\text{hot}} = 2.0$ . These models give a slope to the faint end of the galaxy luminosity function,  $\alpha \approx -1.5$ . More recent models such as that of Bower et al. (2006) have used  $\alpha_{\text{hot}} = 3.2$  for a good match to the  $b_J$  and  $K$ -band galaxy luminosity functions. These can be compared with our exponents from the previous paragraph,  $\alpha_{\text{hot}} = 4.8$  and  $\alpha_{\text{hot, TF}} = 2.5$ , which bracket the value used by Bower et al. (2006). For the normalization, Cole et al. (2000) parameters yield  $\beta_{200} = 1.0$  ( $\beta$  for a disc of  $V_d = 200 \text{ km s}^{-1}$ ), whilst the Bower et al. (2006) parameters give  $\beta_{200} \approx 17$  (although this drops to 12 using updated cosmological parameters, see Bower et al. 2012) as compared with our value of  $\hat{\beta}_{200} = 0.31$ . The net mass loading for MW-like galaxies obtained from our simulations is less than that assumed by Cole et al. (2000) by about a factor of 2, and considerably less than that assumed by Bower et al. (2006).

It is also interesting to consider whether the values of  $\beta$  should rise in starburst galaxies, where the star formation rate may be significantly above the normalization of the KS relation. Although our higher star formation rate simulations do show higher values of  $\beta$  (see Appendix A), this is only by a factor of 2, with  $\beta$  still falling at high gas surface densities. This suggests that the mechanism for

galaxies to stay at high mass loadings is to remain in a state with relatively low surface densities (e.g. Read, Pontzen & Viel 2006).

An alternative formulation of feedback in semi-analytics, suggested by Bower et al. (2012), is to attempt to match only the observable portion of the stellar mass function rather than trying to match a slope that goes to arbitrarily faint galaxies. For example, a model with a constant wind speed (from the disc) ultimately produces a faint end slope that is identical to that of the halo mass function. In an intermediate-mass range, however, the effects of the gravitational potential cause material to be recycled back into the galaxy, producing a characteristic flat portion to the galaxy stellar mass function. By tuning the value of the wind speed, a nearly flat stellar mass function can be achieved over a restricted range. Although this mechanism cannot be extended to arbitrarily faint galaxies (which may be suppressed by other mechanism, e.g. by re-ionization), it does provide a good fit to the observations with a constant  $\beta \approx 8$  over this portion of the mass function.

In contrast to some of the predictions of semi-analytic models are the smaller estimates for the normalization for mass loading found by hydrodynamic simulations. Oppenheimer et al. (2010) use  $\beta = 2$  and  $v_{\text{wind}} = 680 \text{ km s}^{-1}$  to recreate the  $z = 0$  mass function. These simulations are at low resolution with the wind particles partially decoupled from the surrounding gas, making them more comparable to semi-analytic models. Fully hydrodynamical simulations where the wind is coupled to the surrounding ISM are much harder to interpret. Resolution of these issues is beyond the scope of this paper, but better understanding of the differences between semi-analytic models and hydro simulations is clearly required.

In terms of the observed MW, Wakker et al. (2008) estimate the mass accretion rate to be  $0.4 \text{ M}_{\odot} \text{ yr}^{-1}$  from infalling high-velocity clouds. If this is to be combined in a steady-state model of an MW with non-negligible star formation, then  $\beta_{200} \lesssim 0.4$ , so there is some tension between the observed star formation of the MW and the semi-analytic models that would reduce its baryon fraction, and our simulations lie nearer the low observed estimates.

One option is that the semi-analytic models consistently overestimate the  $\beta_{200}$  required. In particular, there are significant degeneracies between  $\beta_{200}$  and the exponent  $\alpha_{\text{hot}}$ . Moreover, many models assume that the wind scaling has a fixed energy efficiency ( $\eta_{\text{T}}$ ) and do not correctly account for the recapture of gas ejected from low-mass galaxies (see Bower et al. 2012 for further discussion). It is entirely plausible that a careful search of parameter space may reveal strongly mass-dependent solutions much closer to those found here.

On the hydrodynamical side, there are a number of physical processes that we neglected that may nevertheless be important. In terms of the gas phases we have included, the inhomogeneous metallicity will make an adjustment to the cooling, and larger scale effects such as a full 3D galactic potential along with shear and features such as bars and spiral arms will also play a role in shaping the ISM. However, it is not apparent why either of these effects will change the overall mass leaving the disc. In terms of the stellar populations we could explore the star formation distribution in terms of the correlation with molecular clouds and also the clustering of stars, which may allow the explosions to strip more material, but this is unlikely because SNe are delayed sufficiently to diffuse out of their parent clouds. The large-scale radiation field may provide an additional mechanism to accelerate the wind (Murray et al. 2005; Hopkins et al. 2011), however in our simulations the thermal energy of the hot material in the disc already provides sufficient velocities to escape the disc.

Potentially the largest discrepancy we have identified is the inconsistency of the distribution of SNe with the gas evolution, i.e.

matching the scale height of star formation with the new scale height of the disc. It may even be possible to make the simulations completely self-consistent by matching the star formation rate to the turbulent structure of the ISM, in a manner such as that envisaged by Krumholz & McKee (2005).

Future simulations could also include the cold phase of the ISM by including radiative cooling below  $10^4 \text{ K}$ . On its own this would tend to reduce  $\beta$ , since a cold phase removes material from the warm phase it would not directly increase the mass loading; however, the physics of this brings in other processes such as self-gravity, magnetic fields and cosmic rays (which may be dominant at these scales). Magnetic fields in particular seem a candidate for entraining more material into the wind, although simulations such as Hill et al. (2012) do not find it to play a significant role.

Overall, whilst we will include the above physical processes in future work, we suspect that these processes will not radically alter the mass loading or significantly change the scalings we have found.

## 7 CONCLUSIONS

In this paper, we have constructed numerically well-converged simulations of a simplified two-phase ISM model, in which an initially isothermal and hydrostatic disc gets disrupted and heated by individual SNe. By not simulating the cold phase of the ISM, we avoided the need to introduce significantly more physical ingredients which require heavy algorithmic approximations and/or fragile recipes. By restricting our simulation volume to only a small section of a disc, we achieve subpc resolution, and are able to investigate the dependence of the outflow on the parameters of the disc. We have included fixed gravity corresponding to our hydrostatic initial conditions, star formation that follows the KS relation, hydrodynamics and a cosmological cooling function. On scales outside the volume, the host disc galaxy for this toy model is reduced to the parameters of gas surface density, gas fraction and star formation efficiency normalized by the KS relation.

Our simulations demonstrate the ability of SNe to launch a galactic wind vertically from a disc, although we do not follow the subsequent evolution of the material in the halo. The SNe create a turbulent ISM with very distinct hot and warm phases, due to the strong transition of the cooling function at  $10^4 \text{ K}$ . These phases exist in order of magnitude pressure equilibrium, with the warm material squeezed into dense lumps, and the excess thermal energy of the hot material causing it to accelerate away from the disc. In Section 4.3 we compare this to a rarefaction process, with the hot ISM escaping to an IGM which is comparatively sparse and pressure-free. Such a model naturally leads an outflow with speed increasing with height above the disc but density decreasing.

The hot outflow entrains colder ISM gas from the disc that may have relatively high metallicity. The hot gas rushes past this cloudy medium producing characteristic tails. Such interfaces may be the sites where lower ionization lines are produced. In Section 4.4, we explore this further by calculating the normalized cross-section of different temperature phases in our simulations, where we see that the velocity distribution of the cooler gas is significantly beneath that of the escaping material.

In a given snapshot, the precise features of our simulations vary greatly due to turbulence and the stochastic nature of SNe; therefore, we examine several global properties which are less sensitive, such as the disc pressure, cooling rate as a fraction of the mean energy injection rate, disc scale height and mass ejection. These reveal a disc that rapidly evolves to higher porosity before reaching a state with an approximately constant mass ejection rate.



This evolution of porosity is broadly reminiscent of the model by Silk (2001).

We perform a range of simulations to investigate the dependence of the mass loading on gas surface density, gas fraction and star formation efficiency, and fit the resulting trends with power laws. Our mass loadings lie in the range 0.01–4, suggesting a switch from a low to a high feedback regime at  $V_d \approx 140 \text{ km s}^{-1}$ . We find little dependence on the normalization of the star formation relation but a significant dependence on the gas fraction and surface density. The latter two can be combined to explain the bulk of the trends as depending on the total surface density of the disc. At high surface densities, we find low mass loading and a high effective wind speed. At low surface densities the reverse is true, and there is an additional contribution due to an increase of the fraction of energy radiated by cooling gas. In Section 4.1.1, we present a simple model where SN blasts stall as they run into clouds swept-up by previous explosions that are so dense that they cool very efficiently and predict that the mass loading depends on gas surface density and gas fraction as  $\beta = \dot{\Sigma}_{\text{wind}}/\dot{\Sigma}_* \propto \Sigma_g^{-8/11} f_g^{4/11}$ . These scalings are very close to those we find from simulations with a high star formation rate,  $\beta \propto \Sigma_g^{-0.82} f_g^{0.48}$ , and weaker (in terms of surface density) than that for the pure Kennicutt relation,  $\beta \propto \Sigma_g^{-1.15} f_g^{0.16}$ . Our prediction for the mass loading in the solar neighbourhood is that each SN results in an ejection of around  $50 M_\odot$  of gas, or  $\beta \sim 0.5$ , slightly above 0.3, the average for the MW as a whole.

The relationship between the wind velocity and the thermalization efficiency exhibits a more complex relationship to the disc properties than that of the mass loading. The thermalization efficiency appears to show a dependency on both the surface density and the gas fraction, and correspondingly the wind velocity does not show a straightforward power law implied from a constant efficiency model. For high surface densities and low gas fractions, an approximate 40 per cent of the injected energy is converted into the outflow's thermal, turbulent and kinetic energy components, although we will underestimate the cooling outside our simulation volume.

We employ the scaling relation obtained from the simulations to calculate the net mass loading,  $\beta = \dot{M}_{\text{wind}}/\dot{M}_*$ , of an exponential disc galaxy with constant gas fraction. Using the Mo et al. (1998) scaling relation between disc and halo, we obtain a scaling with circular velocity of  $\beta \propto V_d^{-4.8}$ , stronger than either energy or momentum-driven winds. Using the observed Tully–Fisher relation we find a weaker dependence,  $\beta \propto V_d^{-2.5}$ . This compares well with recent semi-analytic models which assume  $\alpha_{\text{hot}} \in [2.0, 3.2]$ .

The normalization of our net mass loading at redshift  $z = 0$  for an MW-like galaxy is significantly lower than that assumed in recent phenomenological models, although these models appear to have some degeneracy between the exponent and the normalization, which we will exploit in future work. Notably the mass loading only increases weakly with star formation rate but decreases strongly with surface density, so for starburst galaxies the feedback may be less efficient. Interestingly, our estimated normalization is comparable with inferred values of outflow for the MW based upon the observed accretion and star formation. If indeed there is a higher mass loading, it will require SNe to heat a larger mass of material to a lower temperature, or for the hot outflow to entrain a larger fraction of the warm ISM gas.

The scaling we find sets the investigation of galaxy winds on a new footing, providing a physically motivated subgrid description of winds that can be implemented in cosmological simulations and semi-analytic models.

## ACKNOWLEDGMENTS

Peter Creasey would like to acknowledge the support of an STFC studentship. The authors would like to thank Martin Stringer, Tom Abel, Crystal Martin, Claudia Lagos and Andrew Pontzen for helpful discussions. We would also like to thank the anonymous referee for comments which substantially improved this paper. The calculations for this paper were performed on the ICC Cosmology Machine, which is part of the DiRAC Facility jointly funded by STFC, the Large Facilities Capital Fund of BIS and Durham University. The FLASH software used in this work was in part developed by the DOE-supported ASC/Alliance Center for Astrophysical Thermonuclear Flashes at the University of Chicago. This research was supported in part by the National Science Foundation under grant NSF PHY11-25915.

## REFERENCES

- Aguirre A., Hernquist L., Schaye J., Katz N., Weinberg D. H., Gardner J., 2001, *ApJ*, 561, 521
- Aguirre A., Schaye J., Kim T.-S., Theuns T., Rauch M., Sargent W. L. W., 2004, *ApJ*, 602, 38
- Aguirre A., Schaye J., Hernquist L., Kay S., Springel V., Theuns T., 2005, *ApJ*, 620, L13
- Baldry I. K. et al., 2005, *MNRAS*, 358, 441
- Baldry I. K. et al., 2012, *MNRAS*, 421, 621
- Balogh M. L., Pearce F. R., Bower R. G., Kay S. T., 2001, *MNRAS*, 326, 1228
- Bett P., Eke V., Frenk C. S., Jenkins A., Helly J., Navarro J., 2007, *MNRAS*, 376, 215
- Bigiel F., Leroy A., Walter F., Brinks E., de Blok W. J. G., Madore B., Thornley M. D., 2008, *AJ*, 136, 2846
- Blanton M. R. et al., 2003, *ApJ*, 592, 819
- Blanton M. R., Lupton R. H., Schlegel D. J., Strauss M. A., Brinkmann J., Fukugita M., Loveday J., 2005, *ApJ*, 631, 208
- Boehringer H., Hartquist T. W., 1987, *MNRAS*, 228, 915
- Booth C. M., Schaye J., Delgado J. D., Dalla Vecchia C., 2012, *MNRAS*, 420, 1053
- Bouche N., Hohensee W., Vargas R., Kacprzak G. G., Martin C. L., Cooke J., Churchill C. W., 2012, *MNRAS*, 426, 801
- Bower R. G., Benson A. J., Malbon R., Helly J. C., Frenk C. S., Baugh C. M., Cole S., Lacey C. G., 2006, *MNRAS*, 370, 645
- Bower R. G., Benson A. J., Crain R. A., 2012, *MNRAS*, 422, 2816
- Bowyer S., Lieu R., Sidher S. D., Lampton M., Knude J., 1995, *Nat*, 375, 212
- Breitschwerdt D., de Avillez M. A., 2007, in Elmegreen B. G., Palous J., eds, *Triggered Star Formation in a Turbulent ISM*, Proceedings of the International Astronomical Union 2, IAU Symposium #237, held 14–18 August 2006 in Prague, Czech Republic. Cambridge Univ. Press, Cambridge, p. 57
- Castor J., McCray R., Weaver R., 1975, *ApJ*, 200, L107
- Cen R., Ostriker J. P., 1999, *ApJ*, 519, L109
- Ceverino D., Klypin A., 2009, *ApJ*, 695, 292
- Chabrier G., 2003, *PASP*, 115, 763
- Chen Y.-M., Tremonti C. A., Heckman T. M., Kauffmann G., Weiner B. J., Brinchmann J., Wang J., 2010, *AJ*, 140, 445
- Chevalier R. A., 1974, *ApJ*, 188, 501
- Cole S., Lacey C. G., Baugh C. M., Frenk C. S., 2000, *MNRAS*, 319, 168
- Cooper J. L., Bicknell G. V., Sutherland R. S., Bland-Hawthorn J., 2008, *ApJ*, 674, 157
- Cowie L. L., McKee C. F., 1977, *ApJ*, 211, 135
- Cowie L. L., Songaila A., Kim T.-S., Hu E. M., 1995, *AJ*, 109, 1522
- Cox D. P., 1972, *ApJ*, 178, 159
- Creasey P., Theuns T., Bower R. G., Lacey C. G., 2011, *MNRAS*, 415, 3706
- Dayal P., Ferrara A., Dunlop J. S., 2012, *MNRAS*, submitted (arXiv:1202.4770)
- de Avillez M. A., Breitschwerdt D., 2004, *A&A*, 425, 899

- de Avillez M. A., Breitschwerdt D., 2005a, *A&A*, 436, 585
- de Avillez M. A., Breitschwerdt D., 2005b, *ApJ*, 634, L65
- de Jong T., Boland W., Dalgarno A., 1980, *A&A*, 91, 68
- Dehnen W., Binney J., 1998, *MNRAS*, 294, 429
- Dekel A., Silk J., 1986, *ApJ*, 303, 39
- Dobbs C. L., 2008, *MNRAS*, 391, 844
- Dubois Y., Teyssier R., 2008, *A&A*, 477, 79
- Durier F., Dalla Vecchia C., 2012, *MNRAS*, 419, 465
- Efstathiou G., 1992, *MNRAS*, 256, 43p
- Efstathiou G., 2000, *MNRAS*, 317, 697
- Elmegreen B. G., Scalo J., 2004, *ARA&A*, 42, 211
- Fall S. M., Efstathiou G., 1980, *MNRAS*, 193, 189
- Finlator K., Davé R., 2008, *MNRAS*, 385, 2181
- Flynn C., Holmberg J., Portinari L., Fuchs B., Jahreiß H., 2006, *MNRAS*, 372, 1149
- Freedman W. L. et al., 2001, *ApJ*, 553, 47
- Fryxell B. et al., 2000, *ApJS*, 131, 273
- Fujita A., Mac Low M.-M., Ferrara A., Meiksin A., 2004, *ApJ*, 613, 159
- Fujita A., Martin C. L., Mac Low M.-M., New K. C. B., Weaver R., 2009, *ApJ*, 698, 693
- Fukugita M., Hogan C. J., Peebles P. J. E., 1998, *ApJ*, 503, 518
- Gent F. A., Shukurov A., Fletcher A., Sarson G. R., Mantere M. J., 2012, *arXiv:1204.3567*
- Gnat O., Sternberg A., McKee C. F., 2010, *ApJ*, 718, 1315
- Guo Q., White S., Li C., Boylan-Kolchin M., 2010, *MNRAS*, 404, 1111
- Hartquist T. W., Dyson J. E., Pettini M., Smith L. J., 1986, *MNRAS*, 221, 715
- Heckman T. M., Armus L., Miley G. K., 1990, *ApJS*, 74, 833
- Heckman T. M., Lehnert M. D., Strickland D. K., Armus L., 2000, *ApJS*, 129, 493
- Hill A. S., Joung M. R., Mac Low M.-M., Benjamin R. A., Haffner L. M., Klingenberg C., Waagan K., 2012, *ApJ*, 750, 104
- Hopkins P. F., Quataert E., Murray N., 2012, *MNRAS*, 421, 3522
- Joung M. K. R., Mac Low M.-M., 2006, *ApJ*, 653, 1266
- Joung M. R., Mac Low M.-M., Bryan G. L., 2009, *ApJ*, 704, 137
- Jubelgas M., Springel V., Enßlin T., Pfrommer C., 2008, *A&A*, 481, 33
- Kahn F. D., 1975, in *Proceedings from the 14th International Cosmic Ray Conference, held in München, Germany, 15–29 August 1975, Volume 11 (Invited Lectures and Rapporteur Papers)*, p. 3566
- Kennicutt R. C. Jr., 1998, *ApJ*, 498, 541
- Krumholz M. R., McKee C. F., 2005, *ApJ*, 630, 250
- Kulpa-Dybel K., Otmianowska-Mazur K., Kulesza-Żydzik B., Hanasz M., Kowal G., Wółtański D., Kowalik K., 2011, *ApJ*, 733, L18
- Larson R. B., 1974, *MNRAS*, 169, 229
- Li C., White S. D. M., 2009, *MNRAS*, 398, 2177
- Lopez L. A., Krumholz M. R., Bolatto A. D., Prochaska J. X., Ramirez-Ruiz E., 2011, *ApJ*, 731, 91
- McCarthy I. G., Schaye J., Font A. S., Theuns T., Frenk C. S., Crain R. A., Dalla Vecchia C., 2012, *MNRAS*, 427, 379
- McCray R., Kafatos M., 1987, *ApJ*, 317, 190
- McKee C. F., Ostriker J. P., 1977, *ApJ*, 218, 148
- Mac Low M.-M., Ferrara A., 1999, *ApJ*, 513, 142
- Mac Low M.-M., Klessen R. S., 2005, *Rev. Modern Phys.*, 76, 125
- Martin C. L., 2005, *ApJ*, 621, 227
- Martin P. G., Schwarz D. H., Mandy M. E., 1996, *ApJ*, 461, 265
- Martin C. L., Kobulnicky H. A., Heckman T. M., 2002, *ApJ*, 574, 663
- Matzner C. D., 2002, *ApJ*, 566, 302
- Mo H. J., Mao S., White S. D. M., 1998, *MNRAS*, 295, 319
- Mo H., van den Bosch F. C., White S., 2010, in *Mo H., van den Bosch F. C., White S., eds, Galaxy Formation and Evolution*. Cambridge Univ. Press, Cambridge, p. 501
- Moster B. P., Somerville R. S., Maubetsch C., van den Bosch F. C., Macciò A. V., Naab T., Oser L., 2010, *ApJ*, 710, 903
- Murray N., Quataert E., Thompson T. A., 2005, *ApJ*, 618, 569
- Navarro J. F., Steinmetz M., 1997, *ApJ*, 478, 13
- Navarro J. F., Frenk C. S., White S. D. M., 1997, *ApJ*, 490, 493
- Okamoto T., Gao L., Theuns T., 2008, *MNRAS*, 390, 920
- Oppenheimer B. D., Davé R., 2006, *MNRAS*, 373, 1265
- Oppenheimer B. D., Davé R., 2008, *MNRAS*, 387, 577
- Oppenheimer B. D., Davé R., Kereš D., Fardal M., Katz N., Kollmeier J. A., Weinberg D. H., 2010, *MNRAS*, 406, 2325
- Peeples M. S., Shankar F., 2011, *MNRAS*, 417, 2962
- Pettini M., Shapley A. E., Steidel C. C., Cuby J.-G., Dickinson M., Moorwood A. F. M., Adelberger K. L., Gialavisco M., 2001, *ApJ*, 554, 981
- Pfrommer C., Enßlin T. A., Springel V., Jubelgas M., Dolag K., 2007, *MNRAS*, 378, 385
- Portinari L., Chiosi C., Bressan A., 1998, *A&A*, 334, 505
- Powell L. C., Slyz A., Devriendt J., 2011, *MNRAS*, 414, 3671
- Press W. H., Schechter P., 1974, *ApJ*, 187, 425
- Read J. I., Pontzen A. P., Viel M., 2006, *MNRAS*, 371, 885
- Read J. I., Lake G., Agertz O., Debattista V. P., 2008, *MNRAS*, 389, 1041
- Reed D. S., Bower R., Frenk C. S., Jenkins A., Theuns T., 2007, *MNRAS*, 374, 2
- Rees M. J., Ostriker J. P., 1977, *MNRAS*, 179, 541
- Reid M. J. et al., 2009, *ApJ*, 700, 137
- Rupke D. S., Veilleux S., Sanders D. B., 2005, *ApJS*, 160, 115
- Saitoh T. R., Makino J., 2009, *ApJ*, 697, L99
- Scannapieco E., Brügggen M., 2010, *MNRAS*, 405, 1634
- Scannapieco C. et al., 2012, *MNRAS*, 423, 1726
- Schaye J., 2004, *ApJ*, 609, 667
- Schaye J., Dalla Vecchia C., 2008, *MNRAS*, 383, 1210
- Schaye J., Aguirre A., Kim T.-S., Theuns T., Rauch M., Sargent W. L. W., 2003, *ApJ*, 596, 768
- Schaye J. et al., 2010, *MNRAS*, 402, 1536
- Scoville N. Z., Sanders D. B., 1987, in *Hollenbach D. J., Thronson H. A. Jr, eds, Astrophysics and Space Science Library, Vol. 134, Interstellar processes; Proceedings of the Symposium, Grand Teton National Park, WY, 1–7 July 1986 (A88-14501 03-90)*. D. Reidel Publishing Co., Dordrecht, p. 21
- Sedov L. I., 1959, in *Sedov L. I., ed., Similarity and Dimensional Methods in Mechanics* translated by Friedman M., Translation edited by Holt M. from 4th Russian edition. Academic Press, New York, p. 191
- Sharma M., Nath B. B., Shchekinov Y., 2011, *ApJ*, 736, L27
- Shen S., Mo H. J., White S. D. M., Blanton M. R., Kauffmann G., Voges W., Brinkmann J., Csabai I., 2003, *MNRAS*, 343, 978
- Shen S., Wadsley J., Stinson G., 2010, *MNRAS*, 407, 1581
- Silk J., 2001, *MNRAS*, 324, 313
- Smartt S. J., 2009, *ARA&A*, 47, 63
- Spitzer L. Jr., 1956, *ApJ*, 124, 20
- Springel V., 2005, *MNRAS*, 364, 1105
- Steidel C. C., Erb D. K., Shapley A. E., Pettini M., Reddy N., Bogosavljević M., Rudie G. C., Rakic O., 2010, *ApJ*, 717, 289
- Strang G., 1968, *SIAM J. Numer. Anal.*, 5, 506
- Strickland D. K., Heckman T. M., 2009, *ApJ*, 697, 2030
- Strickland D. K., Stevens I. R., 2000, *MNRAS*, 314, 511
- Stringer M. J., Bower R. G., Cole S., Frenk C. S., Theuns T., 2012, *MNRAS*, 423, 1596
- Sutherland R. S., Dopita M. A., 1993, *ApJS*, 88, 253
- Swinbank A. M. et al., 2009, *MNRAS*, 400, 1121
- Tasker E. J., Tan J. C., 2009, *ApJ*, 700, 358
- Taylor G., 1950, *R. Soc. Lond. Proc. Ser. A*, 201, 159
- Tescari E., Viel M., D'Odorico V., Cristiani S., Calura F., Borgani S., Tornatore L., 2011, *MNRAS*, 411, 826
- Theuns T., Viel M., Kay S., Schaye J., Carswell R. F., Tzanavaris P., 2002, *ApJ*, 578, L5
- Thornton K., Gaudlitz M., Janka H.-T., Steinmetz M., 1998, *ApJ*, 500, 95
- Toomre A., 1964, *ApJ*, 139, 1217
- Trachternach C., de Blok W. J. G., McGaugh S. S., van der Hulst J. M., Dettmar R.-J., 2009, *A&A*, 505, 577
- Tremonti C. A. et al., 2004, *ApJ*, 613, 898
- Truelove J. K., McKee C. F., 1999, *ApJS*, 120, 299
- Tully R. B., Fisher J. R., 1977, *A&A*, 54, 661
- Veilleux S., Cecil G., Bland-Hawthorn J., 2005, *ARA&A*, 43, 769
- Wakker B. P., York D. G., Wilhelm R., Barentine J. C., Richter P., Beers T. C., Ivezić Ž., Howk J. C., 2008, *ApJ*, 672, 298
- Weaver R., McCray R., Castor J., Shapiro P., Moore R., 1977, *ApJ*, 218, 377
- Weiner B. J. et al., 2009, *ApJ*, 692, 187
- White S. D. M., Frenk C. S., 1991, *ApJ*, 379, 52

- White S. D. M., Rees M. J., 1978, MNRAS, 183, 341  
 Wilman R. J., Gerssen J., Bower R. G., Morris S. L., Bacon R., de Zeeuw P. T., Davies R. L., 2005, Nat, 436, 227  
 Wise J. H., Abel T., 2008, ApJ, 685, 40  
 Wolfire M. G., Hollenbach D., McKee C. F., Tielens A. G. G. M., Bakes E. L. O., 1995, ApJ, 443, 152  
 Yang X., Mo H. J., van den Bosch F. C., 2003, MNRAS, 339, 1057

## APPENDIX A: CONVERGENCE AND PARAMETER FITS

In this appendix we investigate the convergence properties of our simulations, along with the dependence upon some of the numerical and physical parameters such as the box size, simulation end time, the star formation rate, the cooling function and the energy of each SN. We also include evolution graphs showing the fits to the mass loading which are central to this work.

We begin by describing a set of simulations where we run an alternative star formation rate, which is compared to the main set of simulations in Section 5. In this parametrization, the surface density of star formation is

$$\dot{\Sigma}_* = 0.1 \Sigma_g / t_{\text{dyn}} \quad (\text{A1})$$

(more commonly used in cosmological simulations), which is appropriate for a marginally Toomre stable disc (Toomre 1964), i.e. the vertical dynamical time is close to the orbital time-scale. Such prescriptions are discussed thoroughly in Schaye & Dalla Vecchia (2008), where they show that with self-regulating feedback this will recover an approximate KS relation of  $\Sigma_g^{3/2}$ .

If we apply equation (A1) to the warm disc of our initial conditions, however, we generally have a much higher star formation rate due to the short dynamical time, which is equivalent to saying that the H I disc is not Toomre stable. If we substitute in the  $t_{\text{dyn}}$  from equation (20) we have a star formation rate of

$$\dot{\Sigma}_* = 2.6 \times 10^{-3} \left( \frac{f_g}{0.1} \right)^{-1} \left( \frac{\Sigma_g}{10 \text{ M}_\odot \text{ pc}^{-2}} \right)^{1/2} \times \Sigma_{\text{gl}}^{1.5} \text{ M}_\odot \text{ kpc}^{-2} \text{ yr}^{-1}, \quad (\text{A2})$$

which we can see from the leading coefficient is an order of magnitude higher than equation (13), although there is some residual dependence on  $f_g$  and  $\Sigma_g$ . To some extent, however, this simulates the conditions more relevant to a starburst galaxy.

In Fig. A1, we investigate the effect of altering the star formation law from equations (13) to (A1), where the latter in general has much higher star formation rates due to the short vertical dynamical time of the disc. At low gas surface densities, more simulations were possible due to the higher star formation rates. The best fit to the former was given in the main text, whilst the best fit to the latter is

$$\beta \sim (20 \pm 8) \Sigma_{\text{gl}}^{-0.82 \pm 0.07} f_g^{0.48 \pm 0.08}. \quad (\text{A3})$$

The effect of increasing the star formation rate flattens the dependency on  $\Sigma_g$  and increases the dependency on  $f_g$ , very close to the values predicted in equation (29), which is to be expected as gravity is much less important in these simulations (see also the discussion in Section 5). The relative insensitivity of  $\beta$  to the order of magnitude change in  $\dot{\Sigma}_*$  can be explained by the fact that the outflows are normalized by the star formation rate, so although those simulations have much higher outflows, the outflow per SN deviates by a much smaller amount. The higher star formation rate runs can also be seen to have less scatter, as they are less susceptible to the Poisson noise of individual SN events.

Fig. A1 also illustrates the effect of the simulation end time on our estimate for the gas surface density dependency, by varying by  $\pm 3$  Myr the final snapshot which is used to construct the fits for  $\beta$  (for the normal star formation rates). This shows little effect, a result of the outflow rates being (on average) very close to linear in these simulations. We perform a corresponding fit for the fiducial parameters in Fig. A2 where we simulate 100 Myr to check that the outflows we see are not a transient phenomena and continue after the 20 Myr of our simulations. The box width in this simulation was 200 pc, so we expect to see more stochasticity, and indeed we see fluctuations lasting many Myr, such that the outflow estimated from a single 20 Myr window could show a deviation of a factor of a few. This is probably the main reason for the scatter in Fig. 9.

We also test how well our simulations are converged with respect to the resolution by taking one of the high star formation rate runs and re-simulating it at the three resolutions L2, L3 and L4 (corresponding to a cell size of 6.3, 3.1 and 1.6 pc, respectively). In Fig. A3 we show six different parameters, the fraction of surface density ejected, the mean pressure in the simulation volume, rate of cooling (as a fraction of the SN energy injection), the porosity and scale heights of the disc and the wind velocity for three different resolutions. All of these properties appear to be well converged with respect to resolution, with the possible exception of the porosity and the disc scale height at the lowest resolution. With respect to the scale height, it is notable that there is some error even at the initial snapshot due to the coarseness of the grid in this case.

We explore the importance of cooling, both in broad terms about the dependence on the magnitude of the cooling, and also upon our specific choice of cooling function. In Fig. A4, we look at the dependency of  $\beta$  for the previous simulation on the magnitude of the cooling function and for comparison we have included the Sutherland & Dopita (1993) cooling function for low-metallicity plasma, equation (11). The linear regression does indeed show a relationship albeit a weak one, with an exponent of  $-0.28$ . For the Sutherland & Dopita (1993) cooling function we have taken the magnitude of cooling to be that at the minimum, equation (12). The fitted  $\beta$  calculated using this figure is a factor of  $\sim 25$  per cent lower than that using our Heaviside cooling function using the same normalization. This is not quite as strong as the dependence suggested by equation (28), of  $-6/11 \approx -0.54$ .

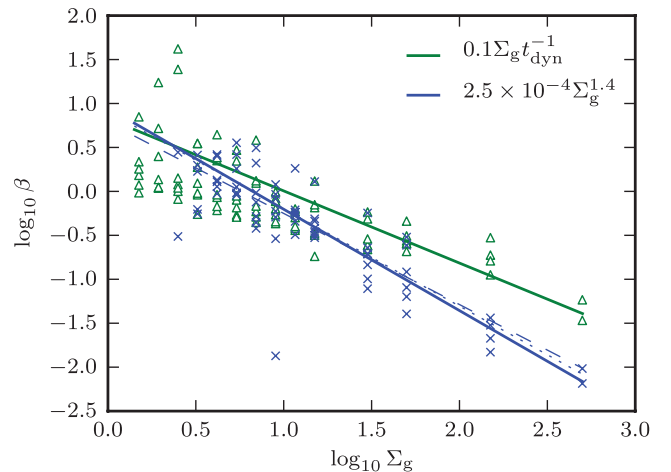


**Figure A1.** Mass loading  $\beta$  as a function of  $\Sigma_g$  for the star formation laws in equation (13) (blue crosses) and equation (A1) (green triangles). Solid lines indicate the best fit for  $f_g = 0.1$  (see the text for exact parametrization). Dashed and dotted blue lines show the fit when varying the end time of the data used for the fit by  $\pm 3$  Myr.



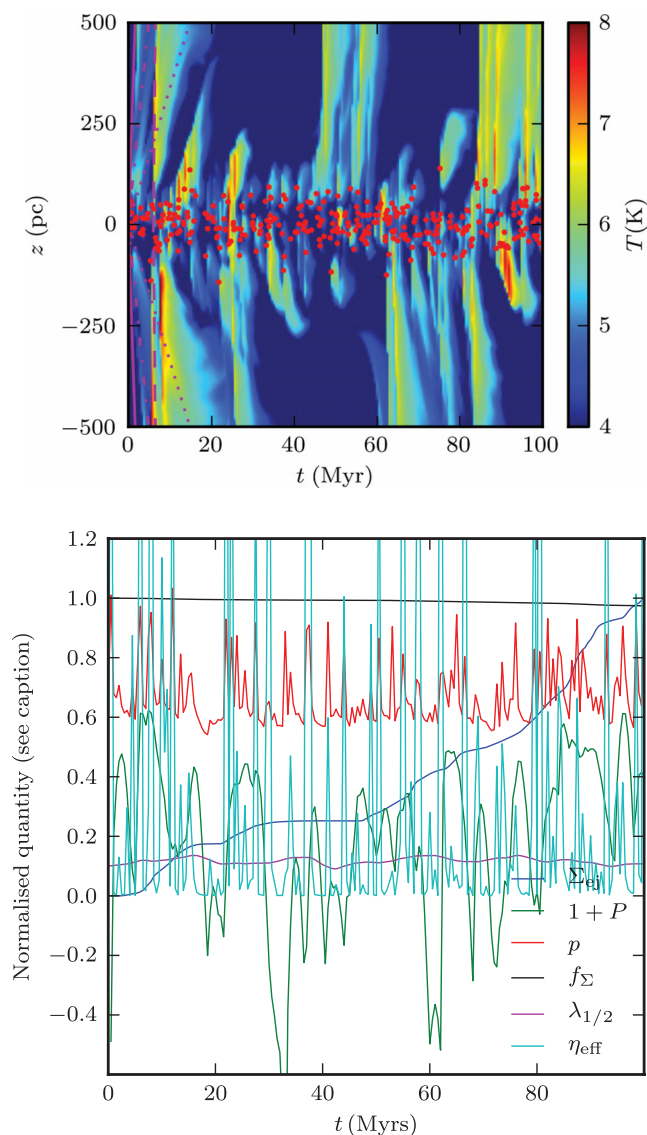


**Figure A2.** Same as for Figs A3 (lower panel) and 4 (upper panel) but for a run of 100 Myr. In the lower panel, the surface density ejected (dark blue line) has been scaled to  $0.3 M_{\odot} \text{ pc}^{-2}$ .

In Fig. A5, we make a further comparison between the Sutherland & Dopita (1993) cooling function and our flat cooling function. We chose the run with the nearest normalization ( $\Lambda = 1.5 \times 10^{-24} \text{ erg cm}^3 \text{ s}^{-1}$ ) to that of the minimum of the Sutherland & Dopita (1993) cooling function (equation 12). We see a very similar phase distribution of the ISM, suggesting that the detailed structure of the cooling function above  $10^4 \text{ K}$  does not play a large role in determining the features of the ISM.

In Fig. A6, we have taken another high star formation rate simulation and adjusted the energy associated with a single SN. Here, we keep the average rate of energy injected per unit time fixed, but inject the energy in more (less) frequent explosions with less (more) energy. The variation between these simulations is surprisingly large: the behaviour of the ISM is indeed quite sensitive to how smooth or stochastic the injected energy is.

In Figs A7 and A8, we investigate the dependence of the simulations on the size of the simulation volume. In Fig. A7, we adjust the vertical size of the simulation volume, i.e. whether increasing the volume to simulate more of the outflow adjusts the dynamics,

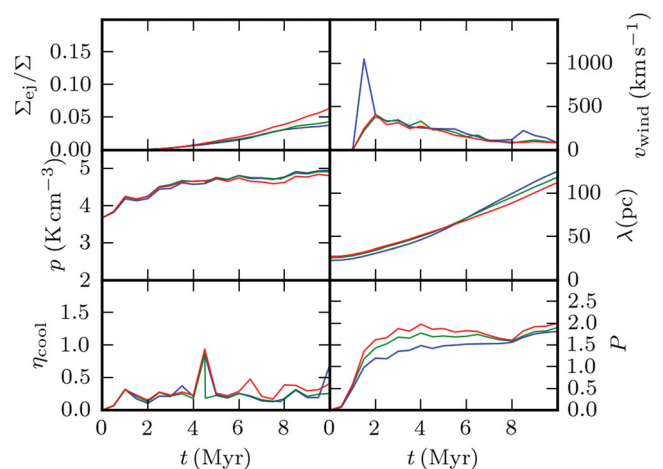


**Figure A3.** Numerical convergence of a high star formation rate run at resolutions L2, L3 and L4 (cell sizes of 6.3, 3.1 and 1.6 pc and shown in red, green and blue, respectively). The upper left-hand panel shows the fraction of gas that has left the simulation volume and the middle left-hand panel indicates the mean pressure in the simulation volume. The lower left-hand panel shows the rate of cooling as a fraction of the mean SNe energy injection rate, the upper right-hand panel shows the mean wind velocity, the middle right-hand panel shows the scale height of the disc and the lower right-hand panel shows the evolution of the porosity in the simulation. The red and green curves follow each other closely, indicating good convergence.

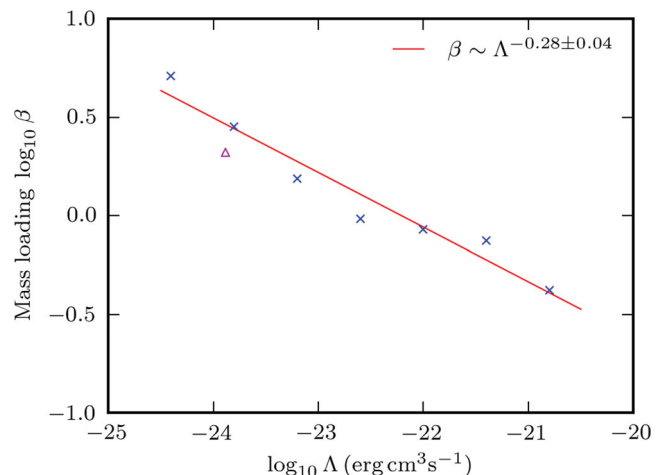


**Figure A4.** Dependence of the mass loading parameter  $\beta$  on the cooling rate. Blue crosses show the estimated  $\beta$  for different values of  $\Lambda$  for Heaviside-shaped cooling function ( $\Lambda = 10^{-22} \text{ erg cm}^3 \text{ s}^{-1}$  is the fiducial value). For comparison, the maroon plus indicates the value of  $\beta$  calculated with the Sutherland & Dopita (1993) cooling function, at the minimum value of this function (equation 12).

for example by allowing some material to fall back to the disc. All parameters are still computed for the original volume ( $\pm 500 \text{ pc}$ ), only the simulation volume has been expanded. All the parameters appear to be almost independent of this change. In Fig. A8, we adjust the horizontal size of simulation volume, where we have multiplied the box width by factors of 2 and 4, respectively. The parameters here also show extremely good convergence, with the larger volumes generally showing less variation in values due to the reduced Poisson noise. The larger volumes also appear to show a marginal reduction in the evolution of the disc scale height.

Finally, in Fig. A9 we have constructed equivalent graphs to that of Fig. 5, but now showing all simulations varying  $\Sigma_g$  and  $f_g$  in Table 1. Each panel shows the time evolution of a single simulation,



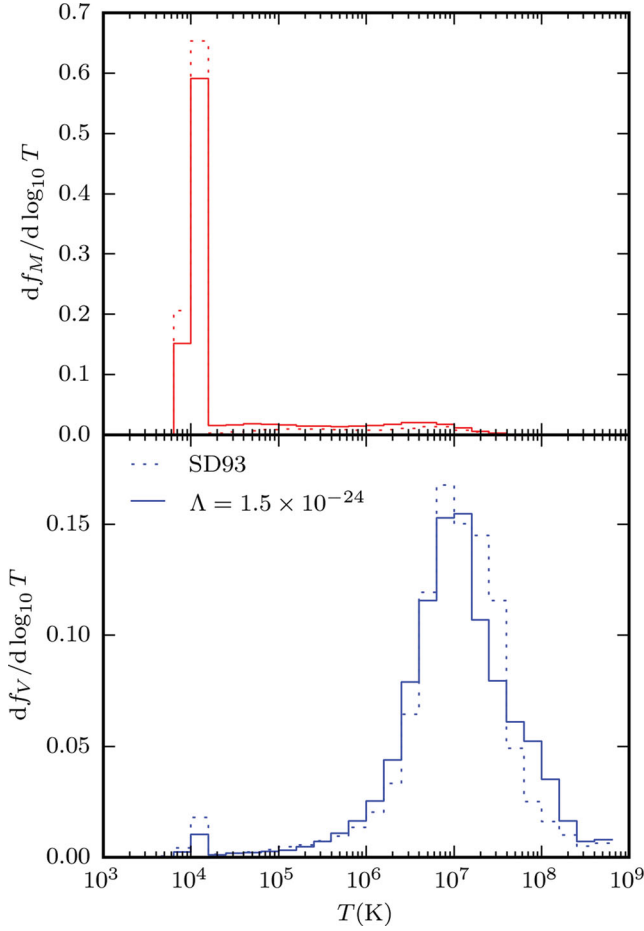


**Figure A5.** Upper panel: mass fraction of the gas in different temperature phases, solid and dashed lines refer to the  $\Lambda = 1.5 \times 10^{-24} \text{ erg cm}^3 \text{ s}^{-1}$  Heaviside cooling function and the Sutherland & Dopita (1993) cooling functions, respectively. The lower panel shows the corresponding volume fractions. The fraction in each phase appears very similar, with the SD93 cooling function showing a slightly narrower temperature distribution of the hot phase by volume.

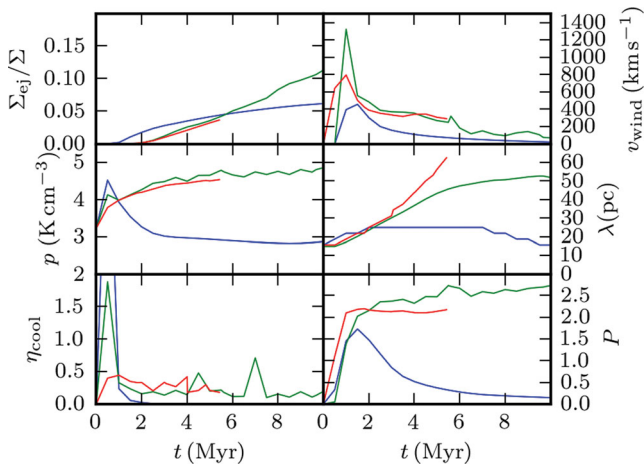


**Figure A6.** Evolution of the simulations as a function of SNe granularity. The green line shows a run with  $10^{51} \text{ erg}$  per SN. The red line is the same simulation, but with  $50 \times$  the frequency of SNe, each releasing  $1/50$ th of the energy ( $2 \times 10^{49} \text{ erg}$ ). The blue line has SNe at  $1/50$ th of the frequency, with  $50 \times$  the energy ( $5 \times 10^{52} \text{ erg}$ ).

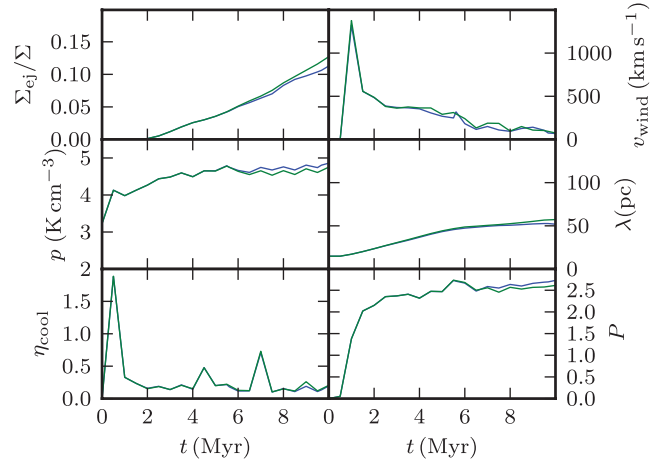


**Figure A7.** Same as Fig. A3, but testing the effect of changing the vertical box size. The blue line is the outflow estimated for a simulation with the fiducial box height (500 pc) and the green line is for 1 kpc.

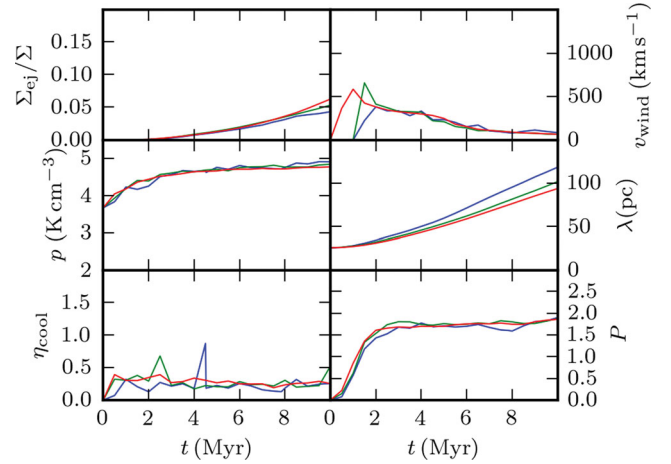


**Figure A8.** Same as Fig. A3, but for three different box sizes. The blue line indicates the run at the L3 resolution, the green line with  $2 \times$  the box width and the red line with  $4 \times$  the box width.

showing the surface density, porosity, instantaneous cooling rate, disc height, mass ejected and pressure, along with a ramp function fit (equation 37) to the mass ejection rates. We can see a strong evolution of the feedback from top left to lower right, i.e. at high surface densities and low gas fractions the simulations develop much stronger mass ejection rates and pressures, and the disc is more heavily disrupted. Note that the mass ejection rate has not been normalized by the surface density, so much of the increase is due to the increased star formation in the higher surface density discs. In a couple of the high surface density panels, the simulation has failed early although there are enough data points to perform a fit to the mass ejection. Although there is considerable stochasticity in the two parameter fits, they seem quite robust.

In conclusion, these studies demonstrate that our simulations are effective at modelling an SN-driven ISM and resilient to changes in numerical parameters. The exact nature of the cooling function exhibits little effect on the disc evolution; in fact, the limiting factor is largely the physical granularity of the discrete SNe and their locations in the disc. To this end, reducing the scatter in our disc property dependencies could be achieved by taking a larger ensemble of runs or alternatively by simulating larger disc areas, either of which increases the total number of SNe introduced.

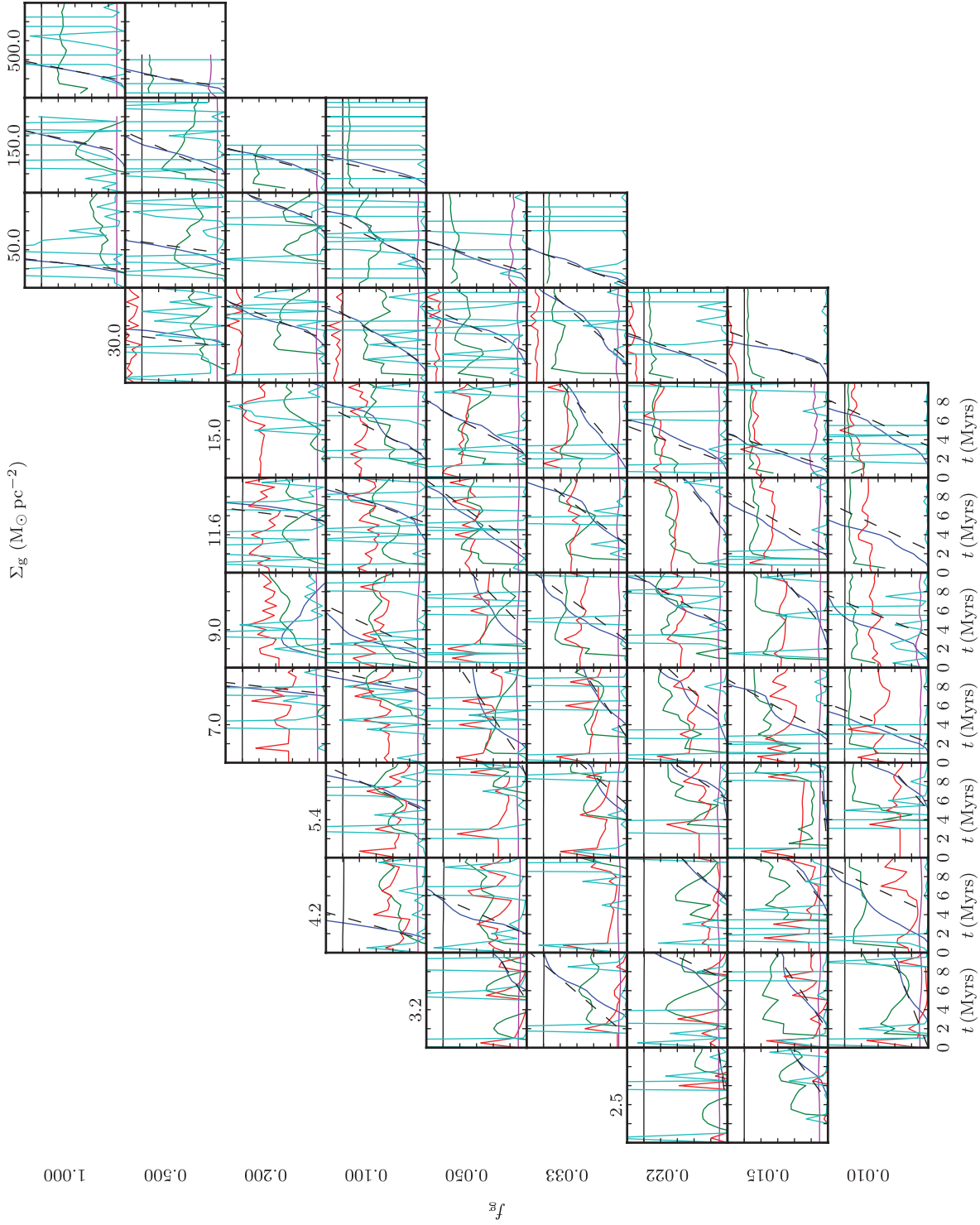


**Figure A9.** Same as Fig. 5, but for all simulations varying  $\Sigma_g$  and  $f_g$  in Table 1. Additional black dashed lines have been added to show a fit to ejection (solid blue lines) given by equation (37).  $\Sigma_{g1} \equiv \Sigma/1 M_\odot \text{ pc}^{-2}$  runs from 1.5 to 11.6 from left- to right-hand panels.  $f_g$  runs from 0.01 to 0.05 from lower to upper panels. Blue line, the amount of gas that has been ejected from the simulation, has now been scaled to units of  $5 M_\odot \text{ pc}^{-2}$  for clarity. Green line shows  $1 + P$ , red line the mean pressure, black line the fraction of gas remaining in the simulation, magenta line the height of the disc and cyan line the very stochastic instantaneous cooling rate as a fraction of the mean SNe energy injection rate.

## SUPPORTING INFORMATION

Additional Supporting Information may be found in the online version of this article:

**Movie.** (<http://mnras.oxfordjournals.org/lookup/suppl/doi:10.1093/mnras/sts439/-/DC1>).

Please note: Oxford University Press are not responsible for the content or functionality of any supporting materials supplied by the authors. Any queries (other than missing material) should be directed to the corresponding author for the article.

This paper has been typeset from a  $\text{\TeX/L\TeX}$  file prepared by the author.